Citation for final published version:

Nowicka, Ewa , Reece, Christian, Althahban, Sultan M., Mohammed, Khaled M. H., Kondrat, Simon A., Morgan, David J. , He, Qian , Willock, David J. , Golunski, Stanislaw , Kiely, Christopher J. and Hutchings, Graham J. 2018. Elucidating the role of CO2 in the soft oxidative dehydrogenation of propane over ceria-based catalysts. ACS Catalysis 8 , pp. 3454-3468. 10.1021/acscatal.7b03805

Publishers page: http://dx.doi.org/10.1021/acscatal.7b03805

Elucidating the role of CO_2 in the soft oxidative dehydrogenation of propane over ceria-based catalysts

Ewa Nowicka,[a,b*] Christian Reece,[a] Sultan M. Althahban,[c] Khaled M. H. Mohammed,[d,e,f] Simon A. Kondrat,[a,g] David J. Morgan,[a] Qian He,[a] David J. Willock,[a] Stanislaw Golunski,[a] Christopher J. Kiely[a,c] and Graham J. Hutchings[a*]

[a] *School of Chemistry, Cardiff University, Main Building, Park Place, Cardiff, CF10 3AT, UK*

[b] *Institut für Chemie, Technische Universität Berlin, Straße des 17. Juni 124, 10623 Berlin, Germany*

[c] *Department of Materials Science and Engineering, Lehigh University, 5 East Packer Avenue, Bethlehem, PA 18015-3195, USA*

[d] *Chemistry Department, Faculty of Science, Sohag University, Sohag, 82524, Egypt*

[e] *UK Catalysis Hub, Research Complex at Harwell, RAL, Harwell, OX110FA, Oxfordshire, UK.*

[f] *Department of Chemistry, University College London, 20 Gordon Street, London WC1H 0AJ, UK*

[g] *Department of Chemistry, Loughborough University, Loughborough, Leicestershire, LE11 3TU, UK*

**Correspondence to Graham J. Hutchings, e-mail: hutch@cardiff.ac.uk and Ewa Nowicka, e-mail: nowickae@cardiff.ac.uk*

Abstract

A mixed oxide support containing Ce, Zr and Al was synthesized using a physical grinding method and applied in the oxidative dehydrogenation of propane using CO_2 as the oxidant. The activity of the support was compared with that of fully-formulated catalysts containing palladium. The Pd/CeZrAlO_x material exhibited long-term stability and selectivity to propene (during continuous operation for 140 h) which is not normally associated with dehydrogenation catalysts. From temperature-programmed desorption of NH_3 and CO_2 it was found that the catalyst possessed both acidic and basic sites. In addition, temperature programmed reduction showed that palladium promoted both the reduction and re-oxidation of the support. When the role of CO_2 was investigated in the absence of gas-phase oxidant, using a Temporal Analysis of Products (TAP) reactor, it was found that CO_2 dissociates over the reduced catalyst leading to formation of CO and selective oxygen species. It is proposed that CO_2 has the dual role of regenerating selective oxygen species, and shifting the equilibrium for alkane dehydrogenation by consuming H_2 through the reverse water-gas-shift reaction. These two mechanistic functions have previously been considered to be mutually exclusive.

Keywords: propane oxidative dehydrogenation, propene, CO_2, Ceria, Pd, Reverse water gas shift

1. Introduction

There is a large and growing worldwide demand for short-chain alkenes, particularly ethene and propene. It is estimated that production of these two chemical building-blocks will exceed 300 M tonne in 2020. In the case of propene, current primary methods for its production (naphtha steam cracking and refinery fluid catalytic cracking) are not sufficient to fulfil the requirements of the market, creating a ‘propene gap’.[1] Therefore, the direct dehydrogenation of alkanes, which is already providing an alternative route to alkenes, is both supplementing and replacing traditional methods as the propene gap widens.[2] However, to obtain high productivity, the dehydrogenation of light alkanes needs to be performed at high temperatures to overcome equilibrium limitations and low rates of reaction. Thus, in turn, drawbacks such as high-energy consumption, low selectivity towards the desired alkene, and accelerated catalyst deactivation are apparent since thermal cracking reactions are favoured at high reaction temperatures. In principle, these obstacles can be overcome by oxidative dehydrogenation (ODH) with molecular oxygen, but despite much work being conducted on developing this technology [3, 4], there are very few examples of commercial ODH processes. The major limitation is that the presence of O_2 often leads to over-oxidation of the alkane, resulting in poor alkene selectivity and a high CO_2 penalty. To overcome these problems, the potential use of ’softer’ oxidants has been evaluated for some time.[5, 6]

Among the soft oxidants, CO_2 has recently received much attention due to the surge in interest in new ways of utilizing this greenhouse gas.[7] Compared with molecular oxygen, CO_2 has many advantages in the process of dehydrogenation: it can minimize over-oxidation of hydrocarbons, therefore enhancing the selectivity for the targeted alkenes; it is also cheap, inert and thermodynamically stable. In view of these advantages, the oxidative dehydrogenation of light alkanes and alkylated aromatics with CO_2 has been arousing considerable interest.[8-13] Although reaction with CO_2 generally leads to lower conversion in comparison to commercialized dehydrogenation processes, the selectivity in a CO_2-ODH reaction is significantly improved.[14, 15]

The mechanism for the ODH of light alkanes with CO_2 has not been thoroughly explained, although different pathways have been proposed. It has been reported that the redox and acid-base properties of oxides can determine which of two pathways the reaction takes.[16] The first route is believed to occur via a Mars-van Krevelen (MvK) mechanism, which involves the participation of lattice oxygen ions as the selective oxygen species, and oxygen vacancies as the adsorption sites. The alternative two-step route is the direct dehydrogenation of the alkane coupled with the reverse water-gas-shift (RWGS) reaction (Eq. 1):

$$\begin{aligned} C_3H_8 &\rightleftharpoons C_3H_6 + H_2 \\ CO_2 + H_2 &\rightleftharpoons CO + H_2O \end{aligned} \qquad \text{(Eq. 1)}$$

The reaction pathway depends on the nature of the catalyst used and the reaction conditions.[17] The MvK mechanism is generally accepted for reactions over metal oxides possessing high oxygen capacity and high redox potential (*e.g.* vanadium oxide or chromium oxide). The presence of gallium oxide or indium oxide is more likely to increase conversion of alkanes due to the RWGS reaction. Both pathways are limited at low temperature: MvK by oxygen mobility; RWGS by thermodynamics. There is, however, a trade-off to operation of the reaction at higher temperatures (>550 °C), which favour combustion of both the reactants and products. Therefore, reducible metal oxides capable of activating CO_2 at lower temperatures could be potential candidates for this reaction.[18]

Cerium (IV) oxide (ceria) is widely used in catalysis, primarily as a component of support materials for metal nanoparticles. However, it has been reported that ceria can be an effective catalyst in its own right for the oxidative dehydrogenation of ethylbenzene to styrene in the presence of CO_2.[19, 20] The high activity of ceria is attributed to its oxygen storage/release capacity (OSC), which is dependent upon the creation and replenishment of oxygen vacancies.[21, 22] The number of potential oxygen vacancies can be further increased and stabilised by the addition of ZrO_2. Such combination of metal oxides leads to higher catalytic performance and a lower temperature for coke oxidation during the regeneration of the spent catalyst. Previous reports have shown that CO_2 can dissociate on the surface on $CeZrO_x$ yielding highly oxidising O species, which maintain Ce in a highly oxidized state.[23] Unfortunately, these materials are not renowned for their durability, and therefore they are often stabilized by using Al_2O_3 as the underlying support. The presence of Al_2O_3 increases the total surface area of the catalyst, which also has been reported to influence catalytic performance in the oxidative dehydrogenation of alkanes.[24] To sum up, the catalytic performance of $CeZrO_x$ materials depends both on their textural properties, such as crystalline phase, particle size and surface area, and on their redox properties.

In this study, a CeO_2-ZrO_2-Al_2O_3 based material, which was synthesized by a mechano-chemical route, was found to be highly selective and durable in the oxidative dehydrogenation of propane (ODP) using CO_2 as a soft oxidant. The subsequent addition of palladium did not reduce the selectivity or durability, but significantly improved the catalytic activity. Conventional characterisation indicates that the role of palladium is to promote oxygen transfer by enhancing the reducibility and re-oxidation of the CeO_2-ZrO_2; while reactive characterisation indicates that the role of CO_2 is to replace the selective oxygen consumed during dehydrogenation and to increase propene formation by shifting the equilibrium through the RWGS reaction.

1. Experimental section

Catalyst preparation

The catalyst supports used in this study were prepared by a physical grinding method. An appropriate amount of the precursors ($Ce(acac)_3$, 1.12 g, 99%, Aldrich and/or $Al(acac)_3$, 99%, Aldrich, 1.66 g and/or $Zr(acac)_4$, 97%, 1.215 g, Aldrich) were added together and ground thoroughly for period of 10 min using a mortar and pestle to form a homogenous powder. The powder was calcined in flowing air at 300°C for 2 h, and heating rate 5˚C/min to give a support composition of Ce: Zr: Al molar ratio 1: 1: 2. Subsequently, Pd was wet impregnated onto calcined support according to the following protocol: H_2O (2 cm^3, HPLC grade, VWR) and an aqueous solution of $Pd(NH_3)_4(NO_3)_2$ (10%, 0.7 cm^3, Aldrich) were added to the support (0.5 g) under vigorous stirring conditions at room temperature to give a catalyst with 5% Pd loading (5%Pd/$CeZrAlO_x$). The solution was agitated in this way until it formed a paste, which was then dried (120 °C, 12 h) and further calcined in flowing air (500 °C, 5 °C min^{-1}, 4 h).

Propane dehydrogenation

Previous reports showed that in the presence of CO_2 and C_3H_8 at a molar ratio of 1:1, the temperature of dehydrogenation can be lowered by 50 °C.[25] We therefore performed all the catalytic studies reported herein utilising a 1:1 ratio between CO_2 and C_3H_8 in the reaction mixture.

Catalytic measurements were performed at atmospheric pressure using a fixed-bed laboratory microreactor, maintaining the gas hourly space velocity (GHSV) at 6000 h^{-1} and total flow rate of gases at 15 cm^3 min^{-1}. Catalyst (0.2 g) was loaded into the reactor tube (length 30 cm, diameter 1.2 cm) and packed between two plugs of quartz wool. The temperature of the catalyst bed was measured with a K-type thermocouple. The inlet gas flow was set using MKS mass-flow controllers. The catalyst was pelletized to give particles in the size range 200-300 µm. Once the catalyst was loaded into the reactor, it was pre-treated prior to reaction in the presence of He for 30 mins at a temperature of 110 °C. Reaction mixtures consisted of He (98%, BOC) CO_2 (99.99%, BOC) and C_3H_8 (99.99%, BOC) with a relative ratio of 26: 37: 37 by volume, unless otherwise stated. The catalyst was in contact with the reaction gas mixture while the reactor was heated from 110 °C to 500 °C. Thermal dehydrogenation was performed under the stream of He and C_3H_8 at 500 °C for 1.5 h. The catalyst was subsequently re-oxidized for 2.5 h in a stream of pure CO_2 at 500 °C, before the standard ODH reaction in the presence of He, C_3H_8 and CO_2 was repeated. The reactants and products were analysed using a Varian 3800 on-line Gas Chromatograph fitted with Porapak Q and Molsieve columns and TCD (CO, CO_2) and FID detectors (CH_4, C_2H_4, C_2H_6, C_3H_6, C_3H_8). Conversion and selectivity was calculated according to equations presented in the Supporting Information. For regeneration of the catalyst, a stream of 15 $cm^3\ min^{-1}$ of CO_2 or He (2.5 h, 500 °C) was used. For the quantification of H_2, a Shimadzu GC-2014 with HaysepQ and Molsieve columns was used. The GC was fitted with TCD & FID detectors and a methanizer.

Catalyst characterization

BET surface area analysis

Surface area measurements were performed using a Gemini 2360 Surface Area Analyser. A 5-point analysis was performed using N_2 as the adsorbate gas. Samples (100 mg) were degassed under a flow of He for 1 h at 120 °C prior to analysis. Surface area analysis of the $Pd/CeZrAlO_x$ material (140 h used and re-oxidized in CO_2) was performed using a Quantachrome, Nova 2200e Surface Area Analyser, using N_2 as the adsorbate gas after degassing the sample for 2 h at 120 °C.

X-ray diffraction (XRD) analysis

XRD analysis was conducted using a PANalytical X'pert pro diffractometer employing a Cu K_α X-ray source. Typical scans were taken over a 2θ angular range between 15 and 80° (1°/min) using 40 kV and 40 mA X-ray source settings. The mean crystallite sizes of Pd and PdO in the samples were estimated using the Scherrer equation.

Thermal gravimetrical analysis (TGA)

TGA was performed using a Perkin Elmer TGA 4000 instrument. The sample was heated from 30 °C to 750 °C at 10 °C min^{-1}, under flowing air (20 cm^3 min^{-1}).

Temperature programmed reduction analysis (TPR)

TPR analyses were performed on a Quantachrome ChemBet. The instrument was calibrated for quantitative measurements of hydrogen consumption using different known masses of CuO wires. These were heated to 600 ^{o}C in an atmosphere of 10% H_2/Ar at a rate of 15 ^{o}C min^{-1}. In all cases, catalysts (0.05 g) were pre-treated in a flow of He at 110 °C for 1 h. TPR analyses were performed using 10%H_2/Ar (BOC 99.9%, 15 cm^3 min^{-1}) over the temperature range 30-750 °C using a 10 °C min^{-1} heating rate. To derive more information from the TPR thermogram, a computed curve was fitted to the experimental one, and the output parameters analysed. A least squares approach was used to compare the computed and experimental profiles. Regression was performed on the experimental curves using least square and a Nelder-Mead Simplex (as described by Lagarias et al.[26]) , algorithm in MATLAB was employed to minimise the variables. Temperature programmed desorption (TPD) analyses were performed on a Quantachrome ChemBet using NH_3 and CO_2 as adsorbates to determine acidic and basic sites, respectively. Prior to analysis, the catalyst surface was saturated with the required gas (NH_3 or CO_2) at room temperature for a period of 30 min, before tracking desorption during heat treatment from 30 to 800 °C in the presence of He.

X-ray photoelectron spectroscopy (XPS) analysis

XPS was carried out using a Kratos Axis Ultra DLD system employing a monochromatic Al K_α X-ray source operating at 120 W. Data were collected with pass energies of 160 eV for survey spectra, and 40 eV for higher-resolution scans. The system was operated in the hybrid mode, using a combination of magnetic immersion and electrostatic lenses, and a signal was acquired by illuminating an area of approximately 300 x 700 μm^2. A magnetically confined charge compensation system was used to minimize charging of the sample surface, and all spectra were acquired with a 90 ° take-off angle. A base pressure of ~ $1x10^{-9}$ Torr was maintained during collection of the spectra.

X-ray absorption fine structure (XAFS) analyses

XAS studies were performed on the B18 Beamline at the UK Diamond Light Source. All samples were formed into compressed pellets using cellulose and the measurements performed in transmission mode with ion chamber detectors. Acquisition of the Ce L3-edge data was performed in a vacuum environment using a Si (111) monochromator, whereas the Pd K-edge and Zr K-edge were obtained by using the Si (311) monochromator. XAS data processing was performed using the Demeter IFEFFIT package.

The Ce L3-edge XANES spectra were fitted using a combination of arctangent (for background subtraction) and Gaussian (for Ce oxidation state) line-shape functions. The data were fitted in the range of $-15 \leq E_o \leq 30$ eV. The spectra were fitted with five Gaussian peaks at fixed eV; namely a high energy peak at 5740 eV (peak A), peaks at 5732 and 5730 eV (peaks B_1 and B_2 respectively), a peak associated with Ce^{3+} at 5728 eV and a pre-edge feature fixed at 5722 eV (peak C), associated with multiple scattering phenomenon with final states having d band character at the bottom of the conduction band of CeO_2.[27] The width of the Gaussian functions was fixed at ~ 3 eV to account for lifetime broadening of a 2p hole state. Ce^{3+} content was determined from the area of the Ce^{3+} peak area [28] as follows:

$$[Ce^{3+}] = \frac{I_{Ce^{3+}}}{I_{B^1} + I_{B^2} + I_A + I_{Ce^{3+}}}$$

EXAFS fitting of the Zr K-edge was used to evaluate two Zr-oxygen (Zr-O_1 and Zr-O_2) distances and their coordination numbers around Zr atom. During the fitting process, the amplitude reduction factor was fixed at a value of 1 and the data were fitted at *k* window = 3 – 12.5 and *r* window = 1 - 3 Å. Also, a Debye-Waller model with a single parameter, at room temperature was used to set the Debye-Waller factor (σ2) parameter during the fitting. For Pd K-edge EXAFS, the data were fitted at *k* window of 3 – 14 and r = 1 – 4 Å. The amplitude reduction factor was constrained at 0.83. EXAFS fitting of the Ce L_3-edge was used to evaluate Ce-O first shell distances and their coordination numbers. Multi-electron excitations were removed prior to EXAFS analysis.[29] During the fitting process, the amplitude reduction factor was fixed at a value of 0.8 and the data were fitted at *k* window = 2.5 – 8.8 and *r* window = 1 - 3 Å. Also, a Debye-Waller model with a single parameter, at room temperature was used to set the Debye-Waller factor (σ2) parameter during the fitting.

Raman spectroscopy

Raman spectroscopy analysis was performed using a Renishaw in Via microscope operated with a green argon ion laser (□=514 nm). A typical spectral acquisition sequence consisted of 10 accumulations of 10 s acquisition time per sample.

Electron microscopy analysis

Samples for examination by scanning transmission electron microscopy (STEM) were prepared by dispersing the catalyst powder (pre-reduced at 500 °C) onto a holey carbon film supported by a 300-mesh copper TEM grid. Bright field (BF) and high angle annular dark field (HAADF) STEM images were taken using an aberration corrected JEM ARM-200CF microscope operating at 200 kV. Samples for analysis by scanning electron microscopy (SEM) and energy dispersive X-ray (XEDS) analysis were prepared by attaching the Pd/$CeZrAlO_x$ catalyst to an Al sample stub using adhesive carbon tape. The samples were examined in a Tescan MAIA3 FEG-SEM operating at an accelerating voltage of 20 keV, which was equipped with an Oxford Instruments silicon drift detector.

Experimental Methods to Determine the Role of CO_2

Temporal analysis of products (TAP)

TAP experiments were performed using a modified TAP-2 system.[30] The catalyst was first reduced by repeatedly pulsing 5% H_2/Ar (99.9 %, BOC) at 400 °C until no more uptake of H_2 was detected. Once the catalyst was reduced, a train of 30 CO_2 (99.99%, BOC) pulses was sent over the catalyst at room temperature, and the exit responses at *m/z* 28 (CO) and *m/z* 44 (CO_2) were recorded. After the pulsing of CO_2, the catalyst was then heated to 400 °C until no further release of CO_2 was detected. This ensured the removal of any surface bound CO_2. The experiment was then repeated but with the catalyst heated to 450 °C after the reduction procedure.

Diffuse reflectance infrared Fourier transform spectroscopy (DRIFTS)

Diffuse reflectance infrared spectroscopy (DRIFTS) was performed using a Bruker Tensor 27 instrument with a HgCdTe (MCT) detector and a Harrick Praying Mantis HVC-DRP-4 cell equipped with ZnSe windows. Gas flows (N_2, (98%, BOC) 10-40 $cm^3\ min^{-1}$, O_2 (98%, BOC)10-20 $cm^3\ min^{-1}$, CO (99.9%, BOC) 0.5-1 $cm^3\ min^{-1}$, and CO_2 (99.99%, BOC)10-20 $cm^3\ min^{-1}$) were regulated by Bronkhorst mass flowmeters. The sample cell was heated in the temperature range 30-350 °C and the analyses were run in the 600-4000 cm^{-1} spectral range, with 64 scans being acquired every 5 mins.

2. Results and Discussion

Catalytic activity

To identify the key interactions between the various components in the Pd/Ce-Zr-Al-O catalytic system, a matrix of materials was initially evaluated at a reaction temperature of 500 ^{o}C (see Table 1, SI-Table S1, Figure S1). Any materials combination without Ce or Pd being present resulted in low activity or poor selectivity. However, both 5%Pd/CeO$_2$ and 5%Pd/CeZrAlO$_x$ showed high conversion levels of propane, but their selectivity patterns differed significantly. While Pd/CeZrAlO$_x$ gave 93% selectivity towards propane, Pd/CeO$_2$ exhibited only 84%, which could be the result of the absence of co-existing basic and acidic sites provided by ZrO$_2$ and Al$_2$O$_3$ in the CeZrAlO$_x$ catalyst support (see below). The Pd-free material (*i.e.,* CeZrAlO$_x$ only) resulted in lower conversion, but a similar selectivity pattern (SI-Figure S1) to the Pd/CeZrAlO$_x$ catalyst. This suggests that Pd was responsible for high conversion, and selectivity was more related to the support composition. Amongst the materials containing different ratios of Ce, Zr and Al, screening studies showed that a support with a composition of Ce$_{0.25}$Zr$_{0.25}$Al$_{0.5}$O$_x$ performed best (SI-Table S1). As the previous studies had been performed with relatively high Pd loading, the effect of varying the loading was initially assessed. This showed that setting the Pd loading below 5% did not increase the activity of the catalyst to a satisfactory level. On the other hand, Pd loadings greater than 5% resulted in improved activity, but also affected selectivity of the material.

Of all the materials tested, 5%Pd/CeZrAlO$_x$ performed the best and was chosen for further investigation and optimisation. We examined the activity of this catalyst over a range of temperatures (450-600 °C). As can be seen in Table 1, the conversion progressively increased as the reaction temperature was increased. However, operation at higher temperatures (*i.e.,* above 500 ^{o}C) adversely affected the product selectivity, which lowered the yield towards propene, leading mostly to formation of undesirable by-products (*i.e.,* CH$_4$ and CO).

Table 1. Propane conversion and propene selectivity of Pd over various Ce based catalyst formulations.
Reaction conditions: 37% C$_3$H$_8$, 37% CO$_2$, 26% He; GHSV=6000 h^{-1}, T = 450 - 600 °C

Material	**Temperature (°C)**	**Conversion* (%)**	**Selectivity* (%)**
Blank	500	0.2	-
CeZrAlO$_x$	500	3	82
5%Pd/Al$_2$O$_3$	500	8.7	64
5%Pd/ZrAlO$_x$	500	3.3	76
5%Pd/CeZrO$_x$	500	10.1	92
5%Pd/CeO$_2$	500	8	84

5%Pd/$CeZrAlO_x$	450	4.7	92
	500	9.5	93
	550	12.3	84
	600	19.8	38
Other catalytic systems			
α-Ga_2O_3 [31]	500[#]	16	89
In_2O_3-Al_2O_3[32]	600[$]	34	72
Cr_2O_3/MCM41[33]	550[£]	40	88

* measured after 1h on stream,
[#] measured at initial activity,
[$] reaction time 2 h,
[£] reaction time 0.17 h

Furthermore, we studied the activity of the 5%Pd/$CeZrAlO_x$ catalyst under reducing conditions, (i.e. in the absence of CO_2) and we refer to this as *thermal dehydrogenation*. The activity of the catalyst decreased rapidly during the first 1.5 h of reaction, although there was small decrease in the selectivity towards propene (Figure 1). The decrease in conversion can be related to the consumption of reactive oxygen species stored within the support, which play a significant role in the first few minutes of the reaction. As these unselective species are likely to be electrophilic, we suggest that they are singly-charged interstitial oxide ions. Because the reaction was performed in the absence of oxidant, both the interstitial oxygen species and the oxygen vacancies formed in the ceria lattice cannot be re-filled from the gas phase, therefore direct dehydrogenation comes into play. As described earlier, the catalyst will behave differently in the presence of an oxidant. It is known that CO_2 will dissociate on the ceria surface forming CO and selective oxygen species which then are capable of refilling oxygen vacancies, thus further facilitating the dehydrogenation reaction. Such a cycle has a positive effect on the product selectivity, as only the selective oxygen species are involved in further reaction. This hypothesis was tested by exposing the catalyst to He and C_3H_8, and then examining if the activity of the material could be restored by re-oxidation with CO_2. As can be seen in Figure 1, not only was the activity of the catalyst restored, but there was also a significant improvement in catalyst selectivity. Under ODH conditions, propene is the main product with CH_4 as the second and only detectable by-product. A full reaction profile of reactions 1 and 2 are shown in the SI (SI-Figures S2 and S3).

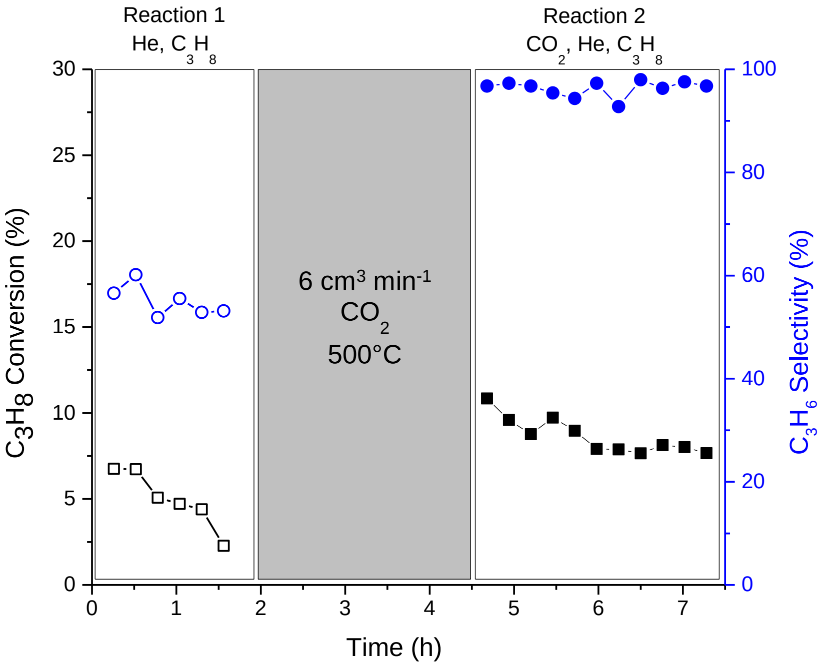

Figure 1. Propane conversion and propene selectivity during thermal dehydrogenation (37% C_3H_8, 67% He; opened symbols: □, ○) and subsequent oxidative dehydrogenation (37% C_3H_8, 37% CO_2, 26%He; filled symbols: ■, ●) after treatment of the 5%Pd/CeZrAlO$_x$ catalyst with CO_2; *Reaction conditions:* GHSV=6000 h^{-1}, T=500 °C.

After showing that catalytic activity can be restored by treatment in the presence of CO_2, we performed a follow-on experiment. First, we carried out the oxidative dehydrogenation of propane in the presence of CO_2, and then further exposed the catalyst to either CO_2 or He, before repeating the ODH reaction to investigate how the intermediate ‘regenerative’ treatment influenced catalyst activity (Figure 2).

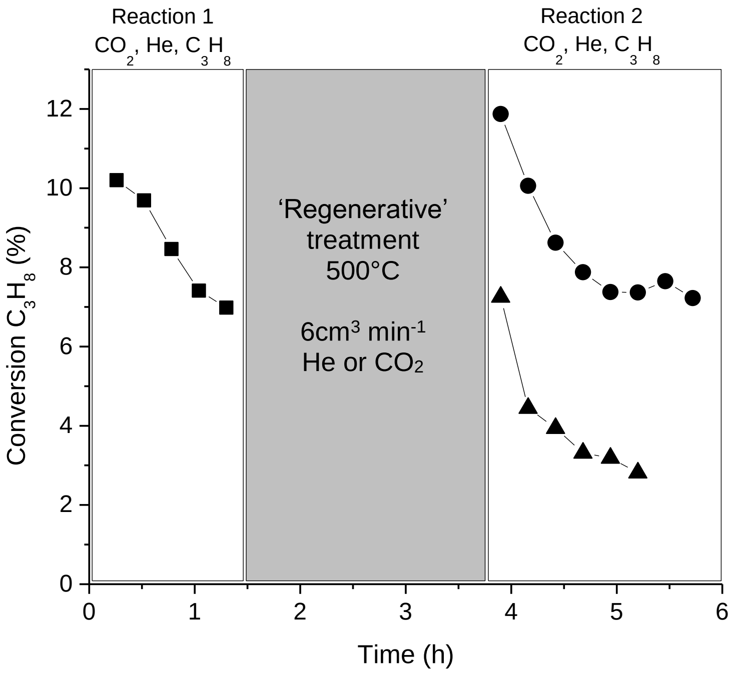

Figure 2. Oxidative dehydrogenation of propane (■, 37% C_3H_8, 37% CO_2, 26% He) and influence on the 5%Pd/$CeZrAlO_x$ catalyst of 'regenerative' treatment methods (under He (▲) or CO_2 (●), flow 6 cm^3 min^{-1}) on the catalytic activity. *Reaction conditions:* GHSV=6000 h^{-1}, T=500 °C

More specifically, two identical batches of the catalyst were prepared and tested in the oxidative dehydrogenation of propane. With the first batch of catalyst, after 1.5 h of the ODH reaction, the gas inlet was switched to pure CO_2 and the catalyst was oxidized in this environment for 2.5 h. Then, the gas flow was changed back to C_3H_8, CO_2, He and the second reaction cycle was performed. In the case of the second batch, after the first ODH reaction, the gas inlet was changed to pure He. The rest of the steps remained the same as for the first batch. Figure 2 shows that under oxidizing conditions, the catalytic activity can be restored, while treatment under reducing conditions did not improve the performance of the material. It is also noteworthy that the activity of the catalyst in the second cycle after contact with CO_2 reached similar level as the first cycle, suggesting that full re-activation of the catalyst had taken place. In addition, the selectivity of the catalyst was improved on moving from reaction 1 to reaction 2. In reaction 1, the initial selectivity to propene was 87.8%, while after CO_2 treatment it reached 94%.

The stability of the catalyst is a major issue in the commercial operation of propane dehydrogenation processes.[34] Most current technologies, which are based on direct (non-oxidative) dehydrogenation, are performed at higher temperatures to achieve cost-effective yields of propene, but this can lead to rapid deactivation of the catalysts through coking. Therefore, in order to maintain a stable yield of propene, the commercial processes requires a number of supplementary operations, *e.g.* addition of steam to the gas-feed (to suppress coking), frequent regeneration of the catalyst, continuous partial replacement of the catalyst, or a rising profile for the operating temperature.[35] Nonetheless, the commercial catalysts generally exhibit relatively short lifetimes, up to a maximum of 3 years.[2]

We have therefore tested our materials for extended periods to observe any changes in catalytic activity. In our investigation, we focused on the selectivity profile since it became quite apparent that the selectivity improves within time-on-stream. The 5%Pd/CeZrAlO$_x$ catalyst exhibited high stability over 140 h of reaction at 500 °C, as shown in Figure 3. Selectivity to propene clearly improved during the reaction whereas the C_3H_8 conversion significantly decreased during the first 1 h of reaction. This is consistent with our interpretation above that unselective oxygen is initially consumed from the catalyst, followed by CO_2 dissociation on the catalyst surface, resulting in the formation of selective oxygen species which are subsequently consumed in the oxidative dehydrogenation reaction. Kovacevic *et al.* have reported a similar observation when studying the effect of morphology on a CeO_2 ODH catalyst in the presence and absence of CO_2.[20] They found that exposure to CO_2 initially led to over-oxidation due to the presence of excess oxygen species triggering the formation of a by-product before reaching stable activity. In our case, it is interesting to note that a gradual decrease of activity to the 4% conversion level was observed, and then relatively stable activity was maintained until the end of the 140 h test. This implies that our 5%Pd/CeZrAlO$_x$ catalyst underwent changes not only during the first hour of the reaction but also during the remaining period of the test. To further understand this aspect, we performed detailed characterization of the 'fresh' and '140 h used' material.

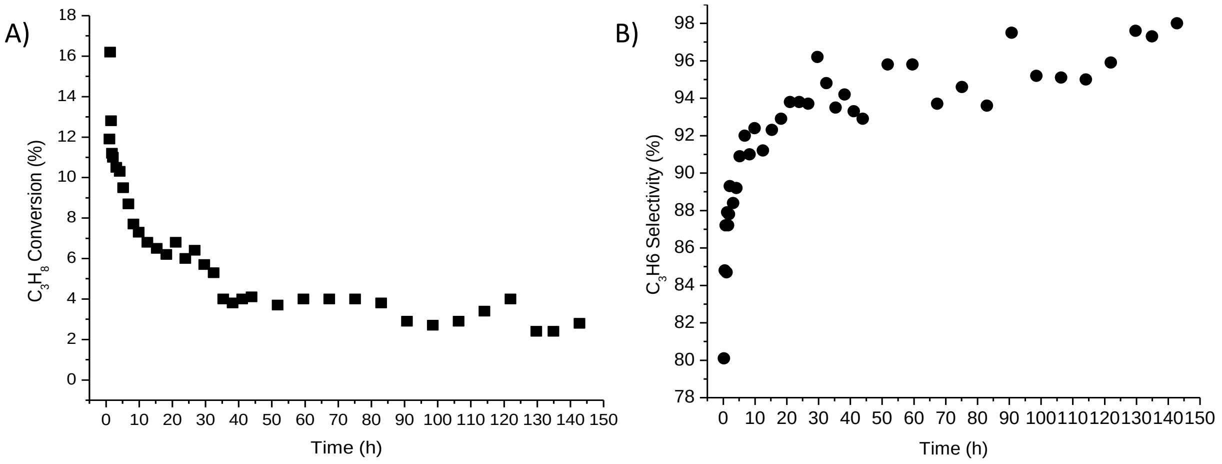

Figure 3. Propane conversion (A) and propene selectivity (B) during oxidative dehydrogenation over an extended reaction period using the 5%Pd/CeZrAlO$_x$ catalyst. *Reaction conditions:* Total flow 15 cm^3/min (37% C_3H_8, 37% CO_2, 26% He), GHSV=6000 h^{-1}, T=500 °C.

Structural characterization of the catalysts

We have carried out detailed textural and structural characterisation in order to understand the promoting effect of Pd on the CeZrAlO$_x$ material. BET surface area data of the fresh and used Pd impregnated CeZrAlO$_x$ catalysts are presented in Table 2. The surface area of the 5%Pd/ CeZrAlO$_x$ catalyst decreased by 41%, whereas a more substantial change was found for the sample after 140 h of testing with the surface area having decreased by 68% compared to the fresh catalyst (Table 2). Nevertheless, the relatively high retained surface area of the used catalyst may partly explain the stability of the material over the course of the catalytic reaction. After the catalyst had been used for 140 h and then re-oxidized in CO_2, a significant increase in surface area was recorded. This suggests that treatment with CO_2 is needed for restoring catalyst activity and may be related to the removal of deposited carbon from the material. The fact that surface area measured over the 140 h used and re-oxidised sample exceeded the area of fresh sample, must be assigned to the error in analysis estimated to be ± 5%.

Table 2. BET surface area analysis of Pd/CeZrAlO$_x$ catalyst materials.

Material	**State**	**Surface Area / m^2 g^{-1}**
5% Pd/CeZrAlO$_x$	Fresh	117*
	Used (1 h)	69
	Used (140 h)	37
	Used (140 h) and re-oxidized with CO_2	122*

*analysed using Quantachrome, Nova 2200e Surface Area Analyser

XRD analysis of the catalysts revealed the CeZrAlO$_x$ material to have a disordered character (Figure 4). This was the expected outcome of the preparation method, in which metal acetylacetonates precursors are mixed and undergo a calcination step that leads to the acetylacetonates being oxidized and converting to a mixed-metal oxide form. XRD analyses of the material after impregnation with Pd, show relatively broad and low intensity peaks consistent with a modified fluorite-type CeO_2 structure. A lack of highly crystalline phases might be indicative of a high fraction of mobile lattice oxygen in the catalyst. When a used sample (after 4 h reaction) was analysed, some weak additional CeO_2 reflections (at 2□ values of 28.64°, 46.99°) were apparent in the XRD pattern. Palladium was detectable in its ionic form in the fresh catalyst by the presence of peaks at 2□ values of 33.9°, 54.7° and 60.2°, which correspond to the (101), (112) and (200) reflections of PdO. The average PdO crystallite size was calculated to be relatively large at 17.4 nm. Furthermore, in the used sample, the PdO reflections were no longer visible, but were replaced by peaks at 2□ values of 40.3°, 47.8° and 68.4° which correspond to the (111), (200) and (220) reflections of f.c.c. Pd metal (mean crystallite size calculated to be 48.4 nm).

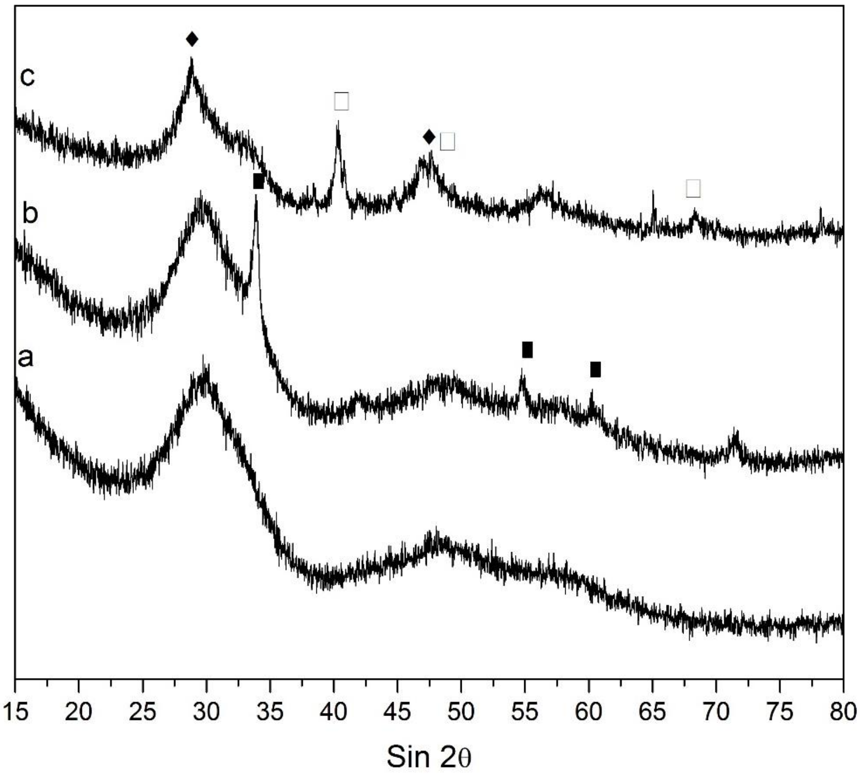

Figure 4. XRD profiles of a) $CeZrAlO_x$, and 5%Pd/$CeZrAlO_x$ in b) the fresh and c) the 4 h used sample (*Key:* ♦: CeO_2, ■: PdO, □: Pd metal)

Since XRD showed that there was an absence of long-range order in the bulk of $CeZrAlO_x$, we used XAFS to probe the local structures of the fresh and used samples of $CeZrAlO_x$ and Pd/ $CeZrAlO_x$, concentrating on the Zr-K, Pd-K and Ce-L3 edge. Firstly, the Zr-K edge data were studied to determine the local structure of Zr and if a solid solution of ceria and zirconia was present in the initial and used catalysts. Figure S4 (Supporting Information) shows the k3-

weighted fittings for the Zr K-edge and the corresponding Fourier transforms derived from $CeZrAlO_x$, Pd-$CeZrAlO_x$ and used Pd-$CeZrAlO_x$ materials. Given that the 1:1 Ce:Zr composition of the samples should result in a tetragonal $CeZrO_2$ type-phase according to well reported phase diagrams,[36, 37] the data was fitted with a model proposed by Prado and co-workers with two different Zr-O distances, indicative of Zr^{4+} being in a distorted tetragonal structure.[38] The rationale for such a fitting is corroborated by the presence of a pre-edge feature (1s to 4d) in the Zr-K edge XANES in all samples (Figure S4), which is sensitive to centro-symmetric distortions, as would exist in tetragonal ZrO_2.[38, 39] However, it was noted that the pre-edge feature was less pronounced than that in a tetragonal ZrO_2 standard, which possibly indicates the presence of some other ZrO_2 character.

Further analysis of the Zr-O first shell fit and comparison with a crystalline tetragonal ZrO_2 standard suggests that the sample is more complex in nature. The calculated Zr-O(2) bond length for $CeZrAlO_x$, fresh Pd-$CeZrAlO_x$ and used Pd-$CeZrAlO_x$ materials can be seen to be notably shorter than in the crystalline tetragonal ZrO_2. Fitting of crystalline monoclinic ZrO_2 can also be performed with two Zr-O distances (Zr-O(2) represents average distance of square plane oxygens and Zr-O(1) those of the triangular coordinate in a Zr coordination polyhedron)[40] and it was found that when using this model, the calculated Zr-O(2) length was comparable with that of all the $CeZrAlO_x$ samples. Therefore, based on first shell fitting, the samples seem to have a more monoclinic type character than tetragonal. As seen from the magnitude of the Fourier Transform of the EXAFS data of crystalline monoclinic and tetragonal phases, the clearest defining difference between the two structures is in the difference in Zr-Zr distances, at 3.46 Å and 4.01 Å for the monoclinic and 3.62 Å in the tetragonal structure.

However, the disordered nature of Zr species in the catalysts, evident from the lack of definable Zr-Zr distances within the Fourier transform data, resulted in no realistic 2nd shell fitting being possible. Given the lack of long range order and non-ideal ZrO_2 bond lengths it is best to describe the sample as being disordered with respect to Zr. Previously reported disordered ZrO_x supported on Al_2O_3 has been found to have comparable EXAFS features to those reported here for the $CeZrAlO_x$ catalysts, specifically monoclinic like 1st shell Zr-O distances and no observable Zr-Zr distances.

Therefore, the reduction in the pre-edge feature could be associated with the local disorder as opposed to the presence of Zr in a cubic structure. Importantly, no notable changes in Zr XANES or EXAFS data were observed between the fresh and used catalysts (SI-Figures S4, S5) showing this level of disorder was retained throughout the reaction.

Unfortunately, due to the close proximity of the Ce L3 and other L edges, extended *k* data could not be acquired for Ce and so only limited EXAFS analysis was possible. The 1st shell Ce-O was fitted to EXAFS data for CeZrAlO$_x$, fresh Pd-CeZrAlO$_x$ and used Pd-CeZrAlO$_x$ material after 4 h reaction time (- an insufficient range in usable *k* data prevented analysis of the 140 h used catalyst). EXAFS fitting considered the presence of multi-electron excitations,[29] which if not accounted for has been shown to give reduced Ce-O distances. However, even when taking multi-electron excitations into account the Ce-O distances observed in all catalyst samples was notably shorter at 2.26(2) Å than seen in CeO$_2$ at 2.34 Å. Shortened Ce-O bond lengths have previously been observed and used as evidence for Ce-Zr-O solid solutions.[41] However, in tetragonal or cubic solid solutions the literature reports first shell EXAFS models having coordination numbers (CN) of 8, while all catalysts prepared in this study had a notably lower CN of *c.a.* 4.5 (Table 3). L3 Ce EXAFS of nanoparticular CeO$_2$ (*c.a.* 2 nm) has been shown to have lower first shell CN of 6 and Ce-O distances between 2.28 and 2.34 Å.[42] The low CN demonstrates local Ce structure is highly disordered according to EXAFS, as with the Zr edge data, and therefore it is difficult to attribute the reduced Ce-O distances to being associated with a solid solution.

Table 3. Ce L3-edge derived EXAFS fitting parameters of catalysts before and after reaction.

Material	Bond	CN	R **(Å)**	**ΔE_0 (eV)**	**σ^2 (Å^2)**	R-factor
CeZrAlO$_x$-fresh	Ce-O	4.6(8)	2.265(20)	2.912(1.538)	0.0071(33)	0.023
Pd/CeZrAlO$_x$-fresh	Ce-O	4.8(7)	2.256(16)	1.736(1.290)	0.0063(27)	0.018
Pd/CeZrAlOx-used 4 hrs	Ce-O	4.0(7)	2.260(18)	0.43(1.583)	0.0049(30)	0.025

Amplitude reduction factor (S$_0^2$) = 0.8, Fit range 2.5-8.8 k and 1- 3 Å R

Despite the disorder seen from the EXAFS, the Ce L3 edge XANES of the CeZrAlO$_x$ catalysts (Figure 5) was clearly identifiable as being CeO$_2$ with varying Ce^{3+} content. Ce L3 edge XANES was therefore used to ascertain the Ce^{3+}/Ce^{4+} content in CeZrAlO$_x$ prior to addition of Pd (Figure 5a), in the fresh Pd-CeZrAlO$_x$ material (Figure 5b) and in the catalyst after 4 h and 140 h time-on-line (Figures 5-c and d, respectively). The XANES of Ce^{4+} in CeO$_2$ is characterised by two white lines arising from many-body final state effects associated with hybridization of Ce 4f and O 2p states.[43] The peak at 5740 eV corresponds to a 2p4f^{0}5d^1 final state (peak A in

Figure 5), while an excitation to 2p4f^{1}5d$^1\underline{L}$ (where $\underline{L}$ denotes a O 2p ligand hole) final state is associated with split peaks at 5732 and 5730 eV (peaks B_1 and B_2 in Figure 5).[27] The splitting of this to 2p4f^{1}5d^{1}L final state is due to crystal field effects. Furthermore, a small intensity peak located at 5722 eV can be assigned to an excitation to a delocalised final state at the bottom of the conduction band of CeO_2 (peak C in Figure 5). In addition to these features which are present in all samples, a band at 5728 eV associated with Ce^{3+} can be seen. The Ce^{3+}/Ce^{4+} content was determined from the spectral weight of Gaussian fitted peak areas and the concentration of Ce^{3+} reported in Table 5. Given the closeness in energy position of B_2 and the Ce^{3+} white line, the Ce^{3+} content of 6% and 8% for fresh $CeZrAlO_x$ and Pd-$CeZrAlO_x$ are considered to be effectively the same within fitting error. As the reaction with propane progresses the determined Ce^{3+} content increased to 23% at 4 h time-on-line and then further increased to 47% at 140 h, clearly demonstrating bulk reduction of the catalyst support during reaction.

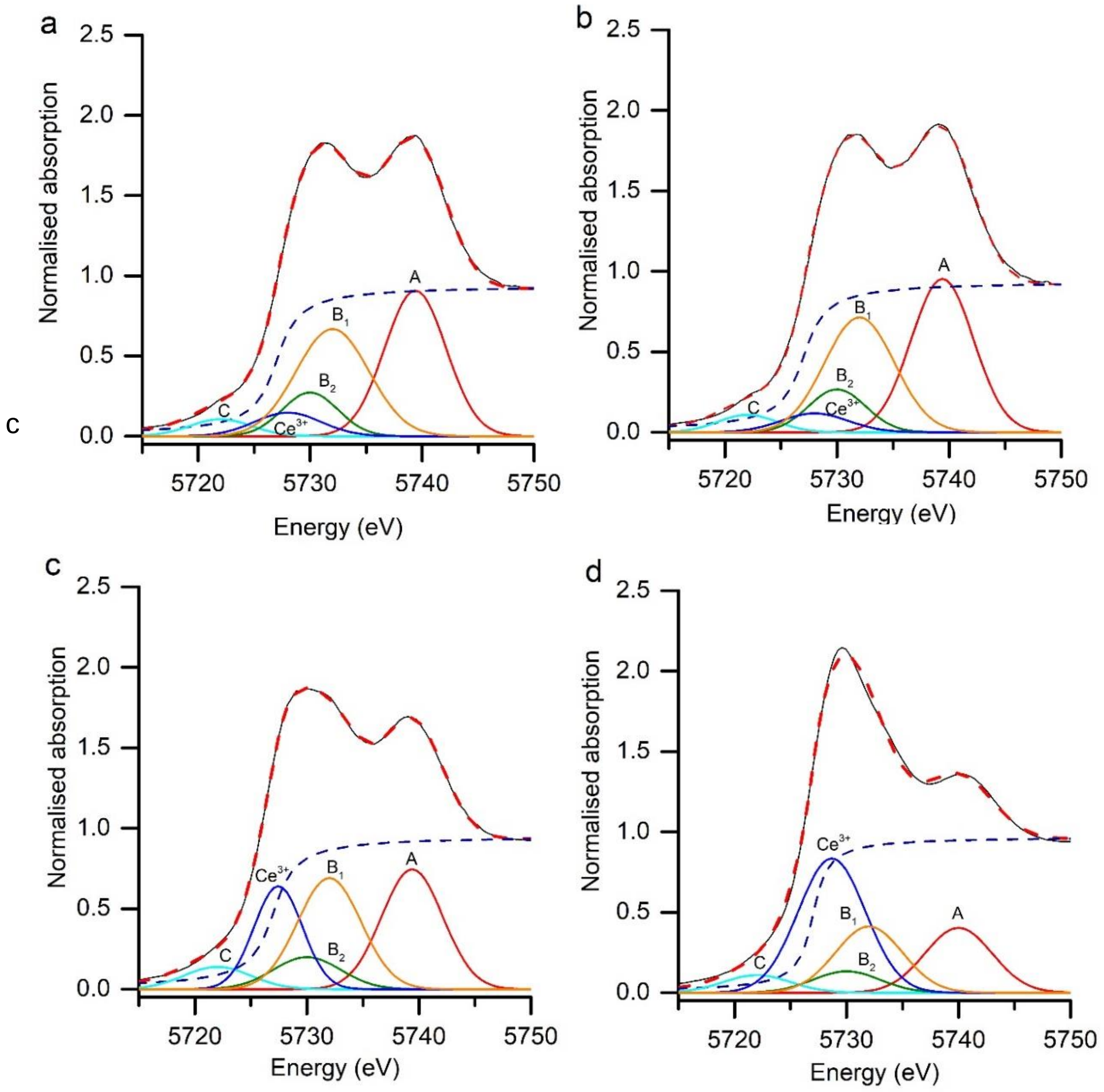

Figure 5: Curve-fitting of the Ce L3-edge XANES spectra for (a) $CeZrAlO_x$, (b) the fresh 5%Pd/$CeZrAlO_x$ catalyst, (c) the 5%Pd/$CeZrAlO_x$ catalyst after 4 h on-line (d) the 5%Pd/$CeZrAlO_x$ catalyst after 140 h on-line. *Key*; Black lines indicate XANES data; red dashed lines the data fit; blue dashed lines the arctangent; red lines - the high-energy transition from a f0 ground state (A); orange lines and green lines - the transition from an f1 ground state (B_1 and B_2). Cyan lines- pre-edge feature from delocalised d like final states (C). Dark blue lines – transitions from Ce^{3+} content within the samples.

In addition, Pd K edge EXAFS (k3 EXAFS) FT data and fitting results are shown in SI-Figure S6 and Table 4, respectively. These clearly show that the PdO present in the fresh Pd-$CeZrAlO_x$ catalyst is reduced to metallic Pd during reaction. The evidence for PdO is constituted by the clear Pd-O distance at 2.01 Å, which is entirely absent from the samples analysed after 4 h and 140 h on-line. In addition, the Pd-Pd distances shorten from those characteristic of PdO_x in the fresh sample to that of f.c.c. Pd metal in the used samples. Also clear from the EXAFS fitting data is an increase in Pd coordination number with time-on-line which is associated with a growth in Pd particle size during reaction.

Table 4: Pd K-edge derived k^3-weighed EXAFS fitting parameters.

Material	bond	N	σ^2 (Å^2)	r (Å)	ΔE_o (eV)	R-factor
Pd/$CeZrAlO_x$-fresh	Pd-O Pd-Pd Pd-Pd	3.8(3) 2.8(9) 4.0(1.1)	0.0022(8) 0.0052(2) 0.0048(2)	2.014(6) 3.041(9) 3.442(7)	-2.421	0.0179
Pd/$CeZrAlO_x$-used 4 h	Pd-Pd	8.5 (2)	0.0080(2)	2.749 (3)	-5.134	0.0037
Pd/$CeZrAlO_x$-used 140 h	Pd-Pd	10.4(5)	0.0068(3)	2.746(2)	-6.942	0.0058

Additionally, XPS analyses of the fresh, used and re-oxidized 5%Pd/$CeZrAlO_x$ samples were performed (Table 5, SI-Figure S7). For the fresh sample, surface Pd is confirmed as being present in an oxidized form (PdO), and most (*ca.*, 90%) of the Ce exists in the higher (4^+) oxidation state. In the used catalyst, after the reduction, the Pd had been converted into its metallic form, with the cerium undergoing partial reduction. These results are in the full agreement with the XAFS analysis. When the reaction was performed for 140 h, even more

Ce^{3+} was present than in the 4 h used catalyst. According to XANES analysis, 47% of the cerium present in the sample is in the 3+ valence state, while from XPS analysis it is only 26.5%. This discrepancy between the numbers can be assigned to the two techniques analysing at different levels with EXAFS analysing all the sample whereas XPS is surface sensitive. In the sample re-oxidized with CO_2, it was noted that the palladium is once again present as PdO, and to the cerium predominantly as Ce^{4+}. This would suggest that co-existence of Pd and Ce in oxidized forms is beneficial for the ODH reaction. Additionally, Pd and Ce must be involved in the catalytic cycle as their presence is crucial in catalysing the reaction. XPS analysis also revealed that re-oxidation by CO_2 does not completely restore the same balance of Ce^{4+} to Ce^{3+} as was found in the fresh sample.

Table 5. XPS analysis of fresh, used and re-oxidized 5%Pd/CeZrAlO$_x$ catalysts.

Material	**Concentration (Atom %)**						**Ce $^{3+}$ (%)**		**Pd**
	Ce	**Zr**	**Al**	**O**	**C**	**Pd**	**XPS**	**XANES**	**Oxidation State**
Fresh	5.6	5.4	6.9	39.0	40.8	2.2	9.6	6	2+
Used 4 h	5.0	4.5	4.6	40.8	41.5	3.6	25.7	23	0
Used, then re-oxidised in CO_2	5.2	5.6	6.0	44.6	34.5	4.2	16.3	-	2+
Used 140 h	4.70	3.0	8.6	35.1	45.0	3.6	26.6	47	0
Used 140 h, then re-oxidized in CO_2	5.80	3.7	11.1	43.3	32.8	3.3	13.0	-	2+

The acid–base properties of the metal oxide catalysts are expected to play a pivotal role in the oxidative dehydrogenation reaction.[44] Higher basicity on the catalyst surface prevents the side reactions by facilitating easier desorption of desired alkenes avoiding further reactions. CO_2 is activated on the acidic sites via the lone pair on the oxygen atom to form unidentate or bidentate complex.[14] The correct balance between basic and acidic sites is therefore extremely important in activating CO_2 and propane. Since the catalyst tested contains CeO_2, ZrO_2 and Al_2O_3, both types of sites are expected to be present in the material. To obtain information concerning the acidic and basic properties of our 5%Pd/CeZrAlO$_x$ catalysts, NH_3 and CO_2-TPD experiments were carried out. The CO_2 and NH_3-TPD profiles of Pd/CeZrAlO$_x$ support are presented in SI-Figure S8. Regarding NH_3-TPD, most of NH_3 desorption occurs between 200 and 500°C (SI-

Figure S8a), indicating the presence of both medium and strong acid sites, respectively. The medium-strength sites are more likely to be associated with the presence of CeO_2 and ZrO_2, while strong acidic sites can probably be assigned to Al_2O_3.[45] The total amount of NH_3 consumed was 2.52 mmol g_{cat}^{-1}.

In terms of CO_2-TPD, three different types of basic sites can be distinguished in Figure S8b-SI. Clear weak basic sites are seen below 200°C (A), followed by a strong signal for CO_2 desorption at 395° C which can be assigned to medium/strong basic sites (B). In addition, a strong desorption peak is visible between 700 and 800°C, clearly demonstrating the presence of strong basic sites (C). The total CO_2 uptake for the analysed catalyst was determined to be 3.48 mmols CO_2 g_{cat}^{-1}.

TPR provided information on the sample reducibility and the influence of palladium on the redox properties of the support. We analysed the reduction properties of $CeZrAlO_x$ and compared it with that of 5%Pd/$CeZrAlO_x$. As presented in Figure 6a, two major reduction peaks were observed for $CeZrAlO_{x.}$ The reduction peak at 474 °C was assigned to reduction of Ce^{4+} at the surface, while that at 633 °C corresponds to the reduction of Ce^{4+} and Zr^{4+} in the bulk.[46] Corresponding TPR analysis of the 5%Pd/$CeZrAlO_x$ sample showed that the presence of Pd shifts the reduction temperature of surface Ce^{4+} sites to lower values implying that a strong interaction between Pd and the support is occurring. Further analysis of the TPR pattern, indicated that signals at 81 and 89°C could be assigned to PdO particles supported on the $CeZrAlO_x$.

As shown in Table 6, for the reduction of the supported PdO particles (peaks 1 and 2), the parameter n in the kinetic expression for the Sestak-Berggren function[47] was calculated to be 0.4 and 1.3 respectively (see SI, section *Temperature programmed reduction: simulation of experimental data*). This indicates that for the lower temperature TPR peak, the reduction of the PdO is the rate limiting step, whereas for higher temperature peak, the H_2 adsorption is the rate limiting step.[48] For both peaks, the γ value of zero indicates that reduction is occurring on either very small PdO particles, or on the edge of already largely reduced metallic particles, as the activation energy does not change with increasing quantity of Pd^0. It can be assumed that the Pd metal is acting a promoter for the reduction of the PdO in both cases, but at higher temperatures the removal of oxygen from the PdO lattice is easier. Peaks 4 and 5 can be assumed to be reduction of $CeZrAlO_x$ support particles that are on the boundary between the reduced Pd particles, as the peak appears at a lower temperature than one would expect the reduction of the bare $CeZrAlO_x$ support to occur, but at a higher temperature than one would expect PdO to still exist.[49] This is also supported by the low value derived for *m* (average 0.3) and the zero value for γ in the kinetic expression. The low *m* parameter indicates that the reduction process is largely unaffected by the reduced material, as Pd^0 would be the site performing the H_2 dissociation, and the zero value of γ indicates that the reduction is within close proximity to the active site. When studying the higher temperature peaks (peaks 6-9), which have been assigned to reduction of bare $CeZrAlO_x$, the decrease in corresponding reduction temperature for the 5%Pd/$CeZrAlO_x$ catalyst indicates that Pd is playing a role in the reduction of bare $CeZrAlO_x$. This hypothesis is supported by the increase in the *m* parameter in peak 6 compared to peak 8, the decrease in the *n* parameter, and lower temperature of reduction. As the previous peak has been assigned to $CeZrAlO_x$ surrounding the reduced Pd particles, it can be hypothesised that the Pd facilitates the reduction of the $CeZrAlO_x$ either by an electronic metal-support interaction or by hydrogen spillover.

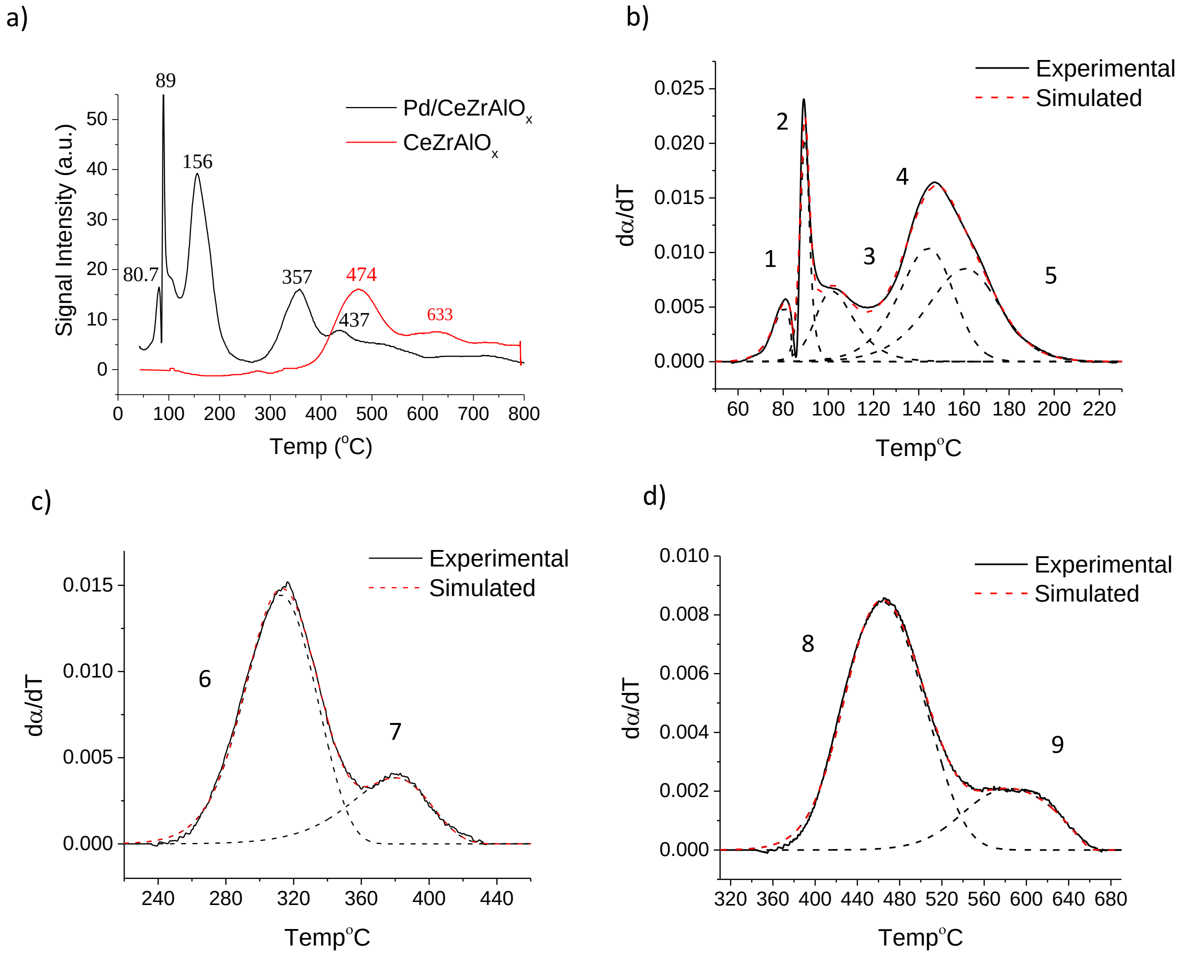

Figure 6. TPR analysis of the $CeZrAlO_x$ and 5%Pd/$CeZrAlO_x$ catalysts. a) Experimentally determined TPR profiles; comparison of experimental and simulation TPR profiles in (b) the 60-220 °C temperature range (5%Pd/$CeZrAlO_x$), c) the 220-440 °C temperature range (5%Pd/$CeZrAlO_x$) and d) the 320-680 °C temperature range ($CeZrAlO_x$).

Table 6. Fitting parameters derived from simulations of the experimental TPR data shown in Figure 6.

Peak No.	m	n	γ	**Proportion (%)**
Pd/$CeZrAlO_x$ (60-220°C)				
1	0.6	0.4	0.00	5.0
2	1.0	1.3	0.00	11.9
3	0.7	1.4	0.03	15.1
4	0.4	1.1	0.00	32.7
5	0.2	1.4	0.00	35.4
Pd/$CeZrAlO_x$ (220-440°C)				
6	0.5	0.9	0.04	76.5
7	0.4	0.9	0.00	23.5
$CeZrAlO_x$ support (320-680°C)				
8	0.3	1.1	0.07	78.4
9	0.4	0.7	0.10	21.6

Electron microscopy analysis

Electron microscopy studies were used to understand the nature and distribution of the Pd component in the 5%Pd/$CeZrAlO_x$ catalyst in the fresh, 4 h used, and used/re-oxidised state. In the fresh state, HAADF -STEM imaging shows that the Pd-containing phase exists as a highly uniform dispersion of 3-5 nm particles on the complex mixed oxide support (Figure 7a). Atomic resolution HAADF images of these nanoparticles in profile view (*e.g.*, Figure 7b) show them to be consistent with the tetragonal PdO phase. XEDS mapping (SI-Figure S9) also shows that the Ce, Zr and Al species are uniformly distributed in the support particles down to the nanometer scale. Such observations are in agreement with the Raman analysis that shows no discrete crystalline ZrO_2 phases or indication of Ce-Zr phase separation (SI-Figure S10).[50] After 4 h of use in the ODH reaction, HAADF-STEM imaging showed that the form of the Pd-containing particles had changed significantly (Figure 8a). The number density of these particles dropped had dramatically due to sintering and their size now spanned the 5-30 nm size range. Lattice image analysis showed that they had completely converted to the f.c.c. metallic Pd phase (Figure 8b) in agreement with the previous XRD analysis (Figure 4).

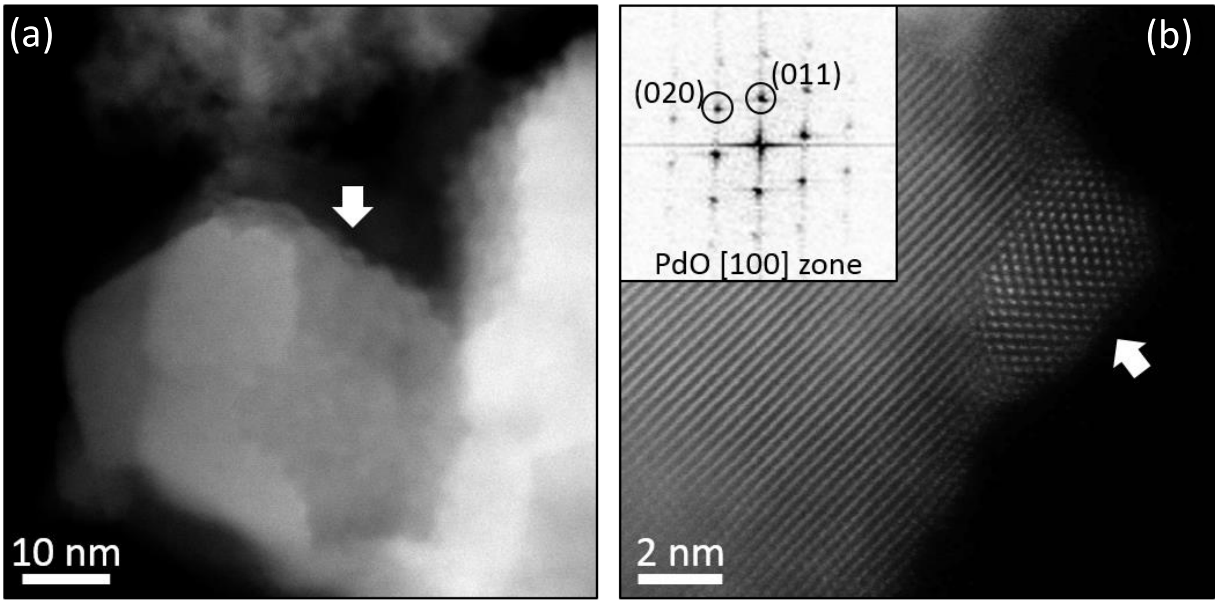

Figure 7. Representative STEM-HAADF images of the fresh 5%Pd/CeZrAlO$_x$ catalyst. (a) A lower magnification image showing ultra-small (3-5 nm) Pd-containing particles (highlighted by the white arrow) in profile view on a CeZrAlO$_x$ support particle. (b) A higher magnification DF-lattice image highlighting one of the particles. The inset shows the Fourier transform obtained from the arrowed particle which matches the tetragonal PdO structure (Ref ICSD 647283) viewed along the [100] zone axis.

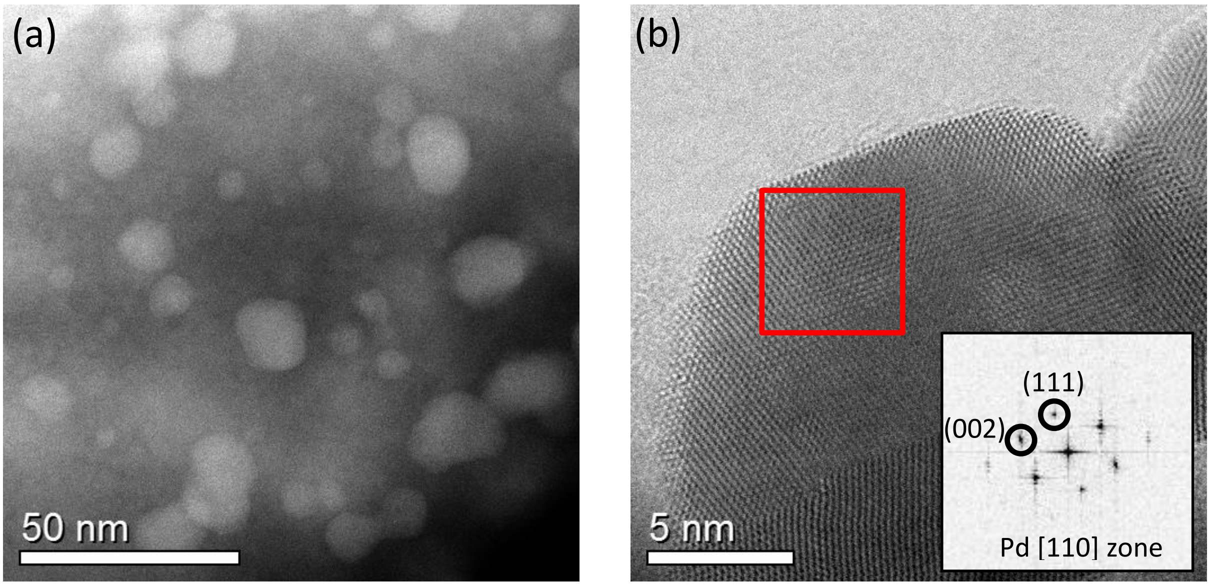

Figure 8. Representative STEM-HAADF images of the ‘4 h used’ 5%Pd/$CeZrAlO_x$ catalyst. (a) A lower magnification image showing 5-30 nm Pd-containing particles dispersed on the $CeZrAlO_x$ support. (b) A higher magnification BF-lattice image of one of the supported particles. The inset shows the Fourier transform obtained from the area highlighted, which matches the f.c.c. structure of metallic Pd (Ref ICSD 648680) viewed along the [110] zone axis.

A sample of the used 5%Pd/$CeZrAlO_x$ catalyst after it had undergone a re-oxidation process in CO_2 was also analysed by electron microscopy. In this case it was not possible to use HAADF-STEM analysis to unambiguously distinguish the Pd-containing from the underlying $CeZrAlO_x$ support by mass contrast (Figure 9a). Instead, we resorted to secondary electron imaging (Figure 9c), local XEDS point spectra (Figure 9b) and complementary XEDS mapping (Figures 9d-g) in the SEM to pick out the Pd-containing particles. This allowed us to determine that the Pd-containing component was now dispersed as large (20-50 nm) PdO particles over the $CeZrAlO_x$ support (once again in agreement with the XRD analysis shown in Figure 4b).

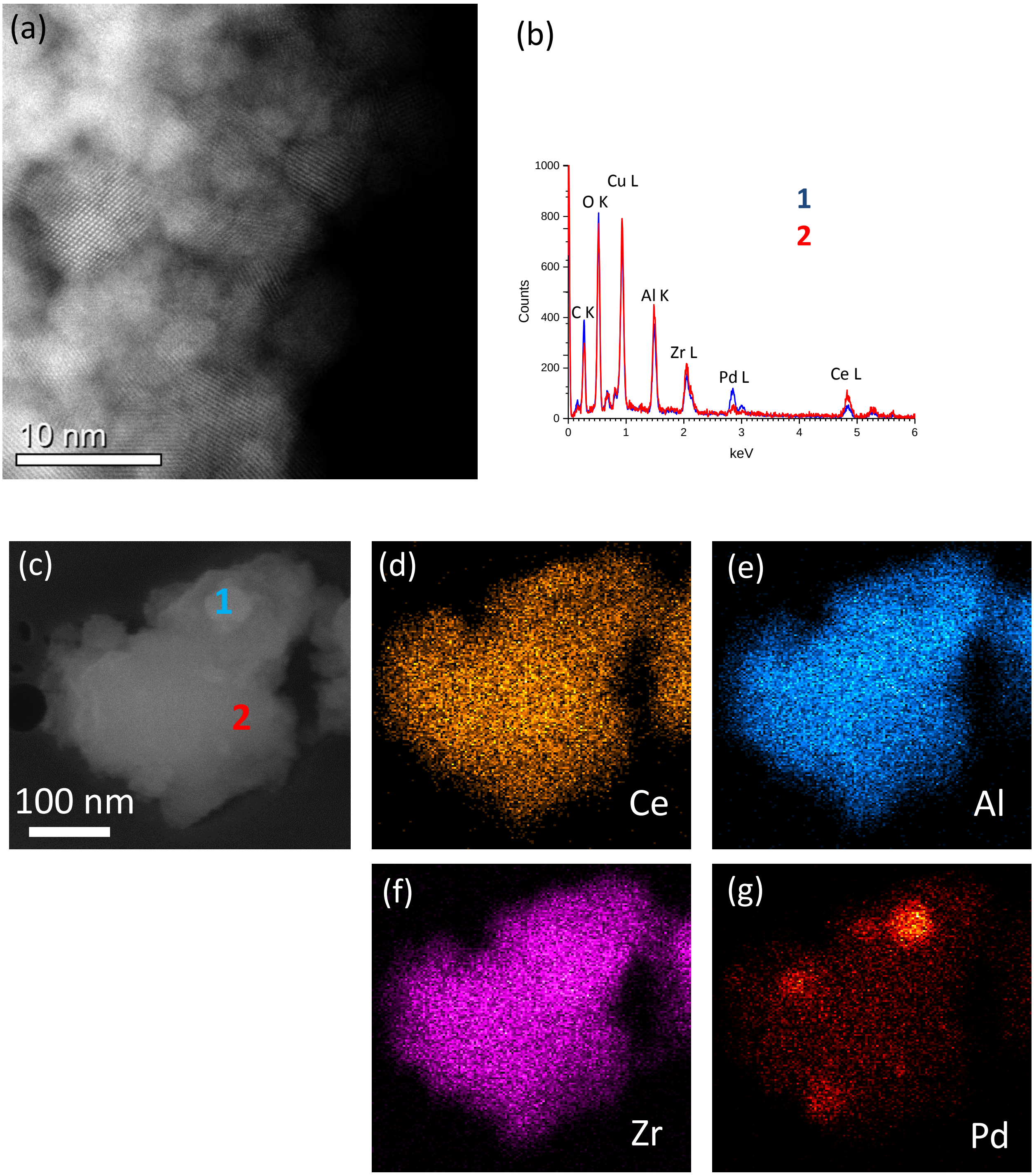

Figure 9. Representative STEM-HAADF image, SE image and XEDS spectra and maps of the ‘4 h used and re-oxidized in CO_2’ 5%Pd/$CeZrAlO_x$ catalyst. (a) An HAADF image showing that any Pd-containing particles, which in this sample will be re-oxidized, are difficult to distinguish from the $CeZrAlO_x$ support by mass contrast. (b) XEDS point spectra acquired from the regions labelled 1 and 2 in the secondary electron image shown in (c) showing that region 1 corresponds to a ~50 nm Pd-containing particle. The corresponding (d) Ce, (e) Al (f) Zr and

(g) Pd XEDS maps of the area shown in (c) confirm that the Pd is now dispersed as large (20-50 nm) PdO particles over the $CeZrAlO_x$ support.

TAP reactor and DRIFT studies to elucidate the role of CO_2 in the reaction mechanism

As described above, our tests with CO_2 present in the gas-feed improved the selectivity of the reaction to propene. When dehydrogenation was performed in the absence of oxidant, the selectivity to methane was relatively high. This indicates that oxygen species from catalyst were consumed in the initial process resulting in the fragmentation of the dehydrogenation product, i.e., propene. Simultaneously, oxygen vacancies formed during the initial step could not be refilled as there was no oxidant available in the gas stream. We also showed that when a reduced catalyst was treated in a flow of CO_2 at 500 °C, the catalytic activity increases, suggesting that oxygen vacancies have somehow been replenished with oxygen facilitating further reaction. This can be rationalized by CO_2 dissociation on the reduced $CeZrAlO_x$ surface, forming CO and additional oxygen species, the latter of which can refill oxygen vacancies. The replenishment of the oxygen species should be therefore independent of the presence of Pd species, since it is mostly related to the oxygen storage capacity of ceria.

To confirm the dissociation of CO_2 on the catalyst surface, CO_2 was pulsed over reduced $CeZrAlO_x$ and 5%Pd/$CeZrAlO_x$ catalysts using a TAP reactor.

The experiment was first performed at room temperature, and it was found that CO_2 irreversibly binds to both materials. It was also found that the 5%Pd/$CeZrAlO_x$ was able to dissociate CO_2 to form CO (Figure 10), whereas the $CeZrAlO_x$ was not (Figure 11), indicating the Pd facilitates the formation of CO at lower temperatures. When the experiment was repeated at a higher temperature (400°C) a stronger CO response was detected in both cases, demonstrating that CO_2 was being dissociated more readily at the higher temperature. The increased temperature also caused the CO_2 adsorption to become reversible, causing the CO_2 response to increase (Figures 10,11).

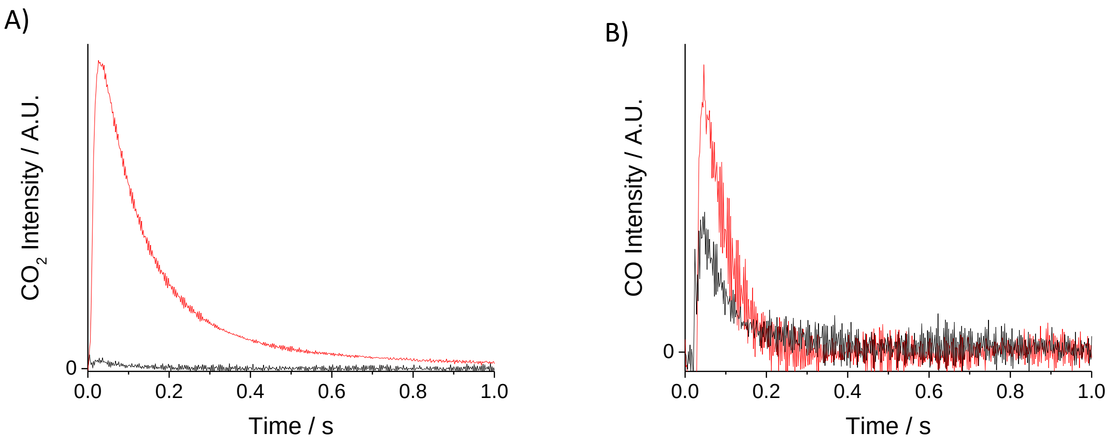

Figure 10. TAP reactor analysis of CO_2 pulsed over the 5%Pd/CeZrAlO$_x$ catalyst. The plots show the signals at (A) *m/z* = 44 and (B) *m/z* = 28 at room temperature (black line) and at 400°C (red line).

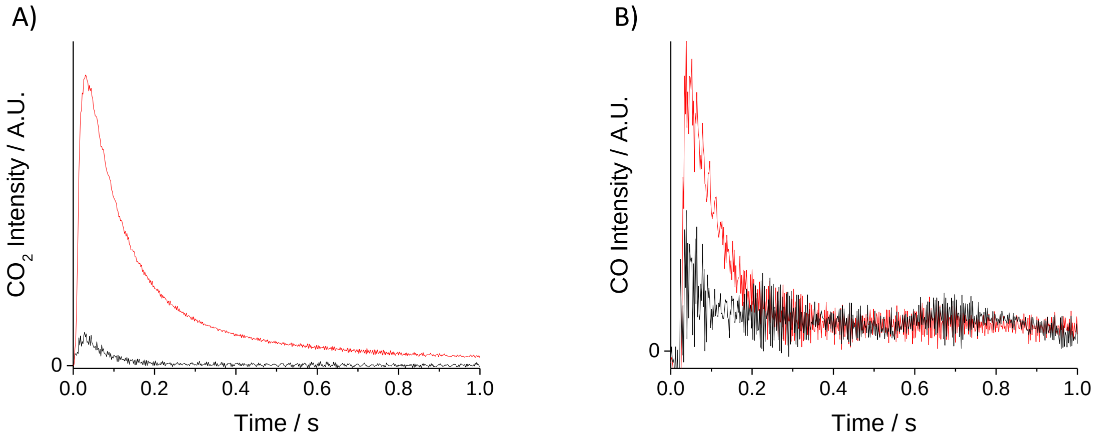

Figure 11. TAP reactor analysis of CO_2 pulsed over the CeZrAlO$_x$ support only. The plots show the temporal signal at (A) *m/z* = 44 and (B) m/z = 28 at room temperature (black line) and at 400°C (red line).

Our TAP experiments clearly show that CO_2 dissociation on a reduced catalyst surface is possible, and that CO species are formed. However, the TAP experiment was performed under high vacuum conditions, so to ensure that the data could be related to the use of the materials at atmospheric pressure, we performed complementary DRIFTS analysis of the 5%Pd/CeZrAlO$_x$. The catalyst was first reduced at 400°C for 4 h in the presence of 5%H_2/Ar and was then divided into two identical batches. The first batch of catalysts was placed in the DRIFTS sample holder and N_2 was flowed over it at 340 °C (Figure 12a). The flow was then changed to 1% CO/N_2 and further scans were taken. From the data shown in Figure 12b, it was found that CO was adsorbed in linear mode on Pd^{2+}/Pd^0, giving a characteristic band at 2150 cm^{-1}. In addition, a strong band at 1934 cm^{-1} is visible, which is assigned to bridging CO adsorption on metallic Pd. The second batch of the reduced catalyst in this experiment was exposed to CO_2. It was first heated to 340°C in N_2 and then the flow changed to 1% CO_2 in N_2. DRIFTS spectra (Figure 12c) show characteristic bands at 2144 and 1932 cm^{-1}, as in the previous experiment with CO gas. Although the bands are weaker than that the in experiment involving CO, they can be easily distinguished in the spectrum, suggesting that CO_2 had dissociated on the surface of the catalyst forming CO, which the further interacted with palladium, giving rise to this strong characteristic signal in the DRIFTS spectra.

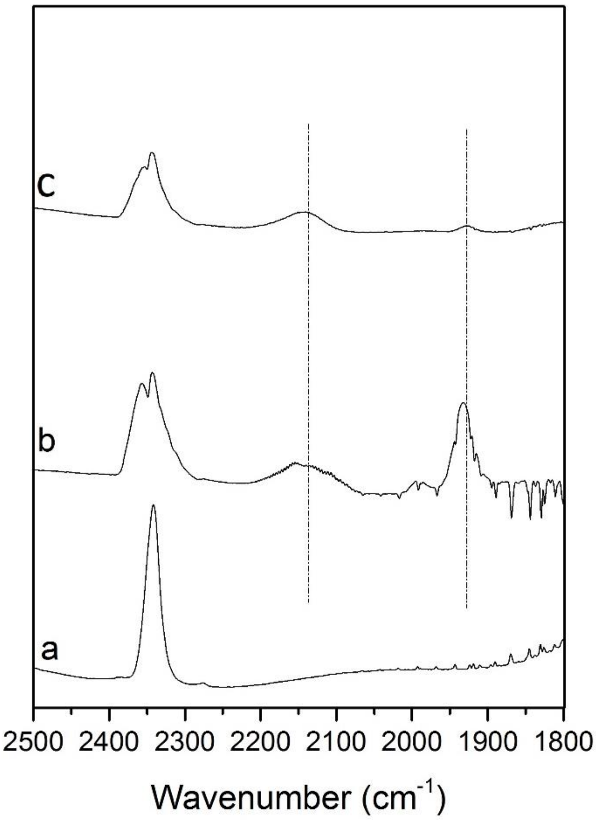

Figure 12. DRIFTS analysis of the 5%Pd/$CeZrAlO_x$ catalyst performed in the presence of a) N_2 only, b) 1% CO/N_2, and. c) 1% CO_2/N_2.

As expected, a similar experiment performed on the fresh (non-reduced) $CeZrAlO_x$ support, did not lead to CO_2 dissociation (SI-Figure S11). It is thus important to consider the role of Pd in CO_2 dissociation. The literature contains reports speculating that ceria alone can dissociate CO_2 to CO without the presence of noble metals.[51] On the other hand, it was reported that when reduced ceria dissociates some CO_2 to maintain a highly oxidized state, migration of O species coming from the ceria-zirconia material towards the active catalytic phase would alter the oxidation state of the palladium, improving catalytic activity.[23] It is possible that CO_2 adsorbs on the peripheral interface sites between Pd and the metal oxide, rather than on Pd only. It has been reported previously that depending on the synthesis techniques and conditions, Pd can be stabilized as ionic species in CeO_2 forming a palladium–ceria interaction phase.[52] Indeed our TPR analysis suggests a close interaction between Pd and CeO_2, supporting the above hypothesis.

As has been stated previously, propane interaction with CO_2 can follow different reaction pathways, amongst which (i) the direct dehydrogenation followed by reverse water gas shift (RWGS) route and (ii) the direct oxidative dehydrogenation (ODH) route are the major ones. In addition, dry reforming of propane, propane cracking and hydrogenolysis reactions may take place.[44] Quantification of the amount of H_2 formed in the overall reaction gives a general idea about the relative contributions from the two major reaction pathways. The obtained volume of H_2 was therefore used to calculate the quantity of C_3H_6 formed in the direct dehydrogenation reaction (TDH), in which propene and hydrogen are formed in equimolar ratios, and do not participate further in the reverse water gas shift reaction. Based on this calculation, the contribution of direct dehydrogenation to the overall propene formation was ~44%. Furthermore, by subtracting the vol % of C_3H_6 generated from TDH from the overall amount of C_3H_6 formed, we estimated the quantity of propane that originates from the oxidative dehydrogenation and direct dehydrogenation coupled with reverse-water gas shift reaction. These two reactions account for ~56% of all propene formed.

Previously been proposed that propane ODH using CO_2 can proceed either via a direct dehydrogenation route coupled with the RWGS reaction, or alternatively via one-step oxidative dehydrogenation.[25] However, the data presented here are consistent with a pathway that includes aspects of both the MvK mechanism and the RWGS reaction. In order for the reaction to follow the MvK mechanism, it needs to possess certain favourable redox properties. In particular, the formation of oxygen vacancies on and near the surface of mixed metal oxides generates active sites and provides a pathway for the transport of lattice oxygen ions. As the number of oxygen vacancies is related to the reducibility of the material, it is often assumed that the number can be calculated from the volume of hydrogen consumed during TPR.[53] Following this line of reasoning, we calculated that the amount of readily accessible oxygen present in the Pd/$CeZrAlO_x$ accounted for 8% of all the oxygen available in the fresh catalyst. However, this does not provide a direct measure of the potential number of oxygen vacancies, because it includes the non-selective (interstitial) oxygen species that are consumed during the initial period of reaction. Collectively, our results indicate that the presence of Pd promotes both the formation of oxygen vacancies and their replenishment with selective (nucleophilic) oxygen ions.

Interestingly the CO_2/CO mass balance was consistently 100% ± 2% during ODH over the Pd/$CeZrAlO_x$, which suggests minimal deposition of carbon on the catalyst during the reaction. This was supported by elemental analysis of the used catalyst after 4 hours of reaction, which showed that the amount of retained carbon was equivalent to only 3.7 % of all the converted propane. Additional TGA analysis showed that even after 140 h of reaction, the amount of carbon deposition was very low (SI-Figure S12). These results infer that an additional function of the Pd is to suppress carbon deposition on the catalyst by enhancing the mobility of the surface oxygen or by promoting the reverse-Boudouard reaction (Eq. 2).

$$C + CO_2 \rightarrow 2CO \qquad \text{(Eq. 2)}$$

Conclusions

The role of CO_2 as a soft oxidant in the dehydrogenation of alkanes over reducible metal oxides has previously been attributed to its ability *either* (i) to re-oxidise the reduced surface as part of an MvK reaction mechanism, *or* (ii) to consume the hydrogen released by direct dehydrogenation through the RWGS reaction. These two pathways have previously been thought to be mutually exclusive. It is worth noting that the RWGS reaction may also proceed by a redox mechanism.[54, 55] Our results indicate that, in ceria-based catalysts such as $CeZrAlO_x$, the MvK and RWGS mechanisms can be linked by a common step. We propose, that lattice oxygen ions abstract hydrogen from the reactant alkane molecules to form the product alkene and H_2O, while the CO_2 replenishes these selective oxygen species, releasing CO into the gas phase (see Figure 13). Although the by-products (CO and H_2O) are also the products of the RWGS, this route to alkenes does not require the stepwise formation of H_2 as an intermediate. The high selectivity to the desired alkene can be explained by the exclusive formation of fully reduced oxygen ions when CO_2 dissociatively adsorbs at surface oxygen vacancy sites. By contrast, the adsorption of O_2 is known to lead to the formation of transient electrophilic oxygen species (such as adatoms, O_2^-, O^-) before O^{2-} ions are formed.[56] Although these electrophilic species are generally short-lived, they account for the formation of CO_2 (and any CO) when O_2 is used as the oxidant.[57]

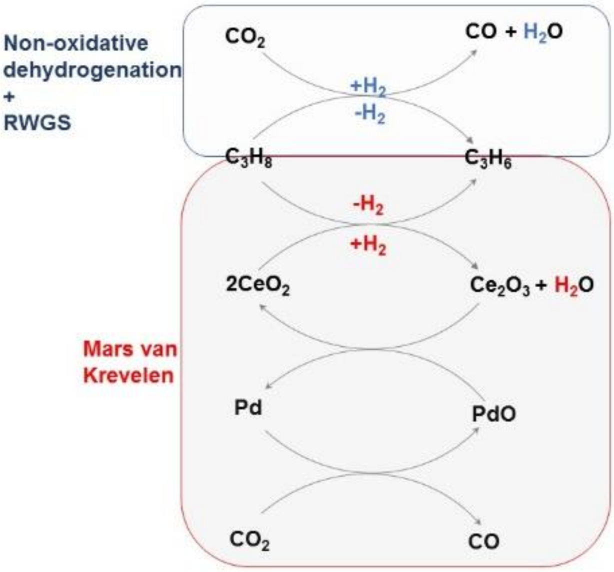

Figure 13. Representative scheme of the reactions involved in the overall ODH process.

The ability of Pd to increase the oxidation activity of redox metal-oxide catalysts is well known [58], and correlates with the observed enhanced reducibility and re-oxidation of the metal oxide surface.[59] This rapid cycle of creating surface oxygen vacancies and then re-filling them from the gas phase prevents the rate of the catalytic reaction becoming limited by the transfer of lattice oxygen ions.[60] However, when O_2 is the oxidant, the presence of Pd promotes the rate of both the selective and non-selective oxidation reactions. By way of contrast, our results demonstrate that when CO_2 is used as the oxidant, the presence of Pd has the critical function of increasing conversion without sacrificing selectivity to propene.

Associated Content

Supporting Information

Catalytic performance calculations; Conversion and selectivity data from catalyst screening experiments; Selectivity profile for the thermal dehydrogenation (TDH) reaction; Conversion profiles for the ODH reaction; EXAFS fitting parameters for Zr K edge; EXAFS data: Zr K-edge, Pd K-edge; XPS spectra; TPD profiles of 5%Pd/CeZrAlO$_x$: Additional SEM-XEDS mapping of 5%Pd/CeZrAlO$_x$, Raman spectroscopy analysis of the CeZrAlO$_x$ support: TPR analysis; simulations of experimental data; DRIFT analysis; TGA analysis.

Acknowledgements

This work was funded by the European Research Council, through the following grant: *After the Goldrush*, ERC-AG-291319. CJK gratefully acknowledges funding from the National Science Foundation Major Research Instrumentation program (GR# MRI/DMR-1040229). We would like to thank Diamond Light Source for use of B18 (SP8071-12), with gratitude to Dr. Diego Gianolio. We would like to acknowledge Dr. Michal Perdjon from Cardiff Catalysis Institute for conducting TG analysis. EN thanks the Technical University of Berlin and Marie Curie-Skłodowska Action for awarding her IPODI fellowship.

References

1. Amghizar, I.; Vandewalle, L. A.; Van Geem, K. M.; Marin, G. B., New Trends in Olefin Production. *Engineering* **2017,** *3*, 171-178.
2. Sattler, J. J. H. B.; Ruiz-Martinez, J.; Santillan-Jimenez, E.; Weckhuysen, B. M., Catalytic Dehydrogenation of Light Alkanes on Metals and Metal Oxides. *Chem. Rev.* **2014,** *114*, 10613-10653.
3. Cavani, F.; Ballarini, N.; Cericola, A., Oxidative dehydrogenation of ethane and propane: How far from commercial implementation? *Catal. Today* **2007,** *127*, 113-131.
4. Carrero, C. A.; Schloegl, R.; Wachs, I. E.; Schomaecker, R., Critical Literature Review of the Kinetics for the Oxidative Dehydrogenation of Propane over Well-Defined Supported Vanadium Oxide Catalysts. *ACS Catal.* **2014,** *4*, 3357-3380.
5. Rozanska, X.; Kondratenko, E. V.; Sauer, J., Oxidative dehydrogenation of propane: Differences between N_2O and O_2 in the reoxidation of reduced vanadia sites and consequences for selectivity. *J. Catal.* **2008,** *256*, 84-94.
6. Wang, S. B.; Zhu, Z. H., Catalytic conversion of alkanes to olefins by carbon dioxide oxidative dehydrogenation - A review. *Energy & Fuels* **2004,** *18*, 1126-1139.
7. Aresta, M.; Dibenedetto, A., Utilisation of CO_2 as a chemical feedstock: opportunities and challenges. *Dalton Trans.* **2007**, 2975-2992.
8. Raju, G.; Reddy, B. M.; Abhishek, B.; Mo, Y.-H.; Park, S.-E., Synthesis of C4 olefins from n-butane over a novel VO_x/SnO_2-ZrO_2 catalyst using CO_2 as soft oxidant. *Appl. Catal. A:Gen.* **2012,** *423*, 168-175.

9. Nakagawa, K.; Kajita, C.; Okumura, K.; Ikenaga, N.; Nishitani-Gamo, M.; Ando, T.; Kobayashi, T.; Suzuki, T., Role of carbon dioxide in the dehydrogenation of ethane over gallium-loaded catalysts. *J. Catal.* **2001,** *203*, 87-93.

10. Takehira, K.; Ohishi, Y.; Shishido, T.; Kawabata, T.; Takaki, K.; Zhang, Q.; Wang, Y., Behavior of active sites on Cr-MCM-41 catalysts during the dehydrogenation of propane with CO_2, *J. Catal.* **2004,** *224*, 404-416.

11. Sugino, M. O.; Shimada, H.; Turuda, T.; Miura, H.; Ikenaga, N.; Suzuki, T., Oxidative Dehydrogenation of ethylbenzene with carbon dioxide. *Appl. Catal. A:Gen.* **1995,** *121*, 125-137.

12. Ansari, M. B.; Park, S.-E., Carbon dioxide utilization as a soft oxidant and promoter in catalysis. *Energ. Environ. Sci.* **2012,** *5*, 9419-9437.

13. Wang, C. H.; Shi, J.; Cui, X. M.; Zhang, J.; Zhang, C. H.; Wang, L. C.; Lv, B. L., The role of CO_2 in dehydrogenation of ethylbenzene over pure alpha-Fe_2O_3 catalysts with different facets. *J. Catal.* **2017,** *345*, 104-112.

14. Mukherjee, D.; Park, S. E.; Reddy, B. M., CO2 as a soft oxidant for oxidative dehydrogenation reaction: An eco benign process for industry. *J. CO_2 Util.* **2016,** *16*, 301-312.

15. Kang, J.; Czaja, A. D.; Guliants, V. V., Carbon Dioxide as Feedstock in Selective Oxidation of Propane. *Eur. J. Inorg. Chem.* **2017,** *2017*, 4757-4762.

16. Sato, S.; Ohhara, M.; Sodesawa, T.; Nozaki, F., Combination of ethylbenzene dehydrogenation and carbon dioxide shift-reaction over a sodium-oxide alumina catalyst. *Appl. Catal.* **1988,** *37*, 207-215.

17. Atanga, M. A.; Rezaei, F.; Jawad, A.; Fitch, M.; Rownaghi, A. A., Oxidative dehydrogenation of propane to propylene with carbon dioxide. *Appl. Catal. B: Environ.* **2018,** *220*, 429-445.

18. Zangeneh, F. T.; Taeb, A.; Gholivand, K.; Sahebdelfar, S., Thermodynamic Equilibrium Analysis of Propane Dehydrogenation with Carbon Dioxide and Side Reactions. *Chem. Eng. Commun.* **2016,** *203*, 557-565.

19. Zhang, L.; Wu, Z. L.; Nelson, N. C.; Sadow, A. D.; Slowing, II; Overbury, S. H., Role of CO_2 As a Soft Oxidant For Dehydrogenation of Ethylbenzene to Styrene over a High-Surface-Area Ceria Catalyst. *ACS Catal.* **2015,** *5*, 6426-6435.

20. Kovacevic, M.; Agarwal, S.; Mojet, B. L.; van Ommen, J. G.; Lefferts, L., The effects of morphology of cerium oxide catalysts for dehydrogenation of ethylbenzene to styrene. *Appl. Catal. A:Gen.* **2015,** *505*, 354-364.

21. Sharma, S.; Hilaire, S.; Vohs, J. M.; Gorte, R. J.; Jen, H. W., Evidence for Oxidation of Ceria by CO_2. *J. Catal.* **2000,** *190*, 199-204.

22. Valenzuela, R. X.; Bueno, G.; Solbes, A.; Sapina, F.; Martinez, E.; Corberan, V. C., Nanostructured ceria-based catalysts for oxydehydrogenation of ethane with CO2. *Top. Catal.* **2001,** *15*, 181-188.

23. Demoulin, O.; Navez, M.; Mugabo, J. L.; Ruiz, P., The oxidizing role of CO_2 at mild temperature on ceria-based catalysts. *Appl. Catal. B: Environ.* **2007,** *70*, 284-293.

24. Wang, T. H.; Guan, X. L.; Lu, H. Y.; Liu, Z. W.; Ji, M., Nanoflake-assembled Al_2O_3-supported CeO_2-ZrO_2 as an efficient catalyst for oxidative dehydrogenation of ethylbenzene with CO_2. *Appl. Surf. Sci.* **2017,** *398*, 1-8.

25. Ascoop, I.; Galvita, V. V.; Alexopoulos, K.; Reyniers, M. F.; Van der Voort, P.; Bliznuk, V.; Marin, G. B., The role of CO_2 in the dehydrogenation of propane over WO_x-VO_x/SiO_2. *J. Catal.* **2016,** *335*, 1-10.

26. Lagarias, J. C.; Reeds, J. A.; Wright, M. H.; Wright, P. E., Convergence properties of the Nelder-Mead simplex method in low dimensions. *Siam J. Optimiz.* **1998,** *9*, 112-147.

27. Soldatov, A. V.; Ivanchenko, T. S.; Della Longa, S.; Kotani, A.; Iwamoto, Y.; Bianconi, A., Crystal-structure effects in the Ce L_3-edge x-ray-absorption spectrum of CeO2: Multiple-scattering resonances and many-body final states. *Phys. Rev. B* **1994,** *50*, 5074-5080.

28. Fernandes, V.; Graff, I. L.; Varalda, J.; Amaral, L.; Fichtner, P.; Demaille, D.; Zheng, Y.; Schreiner, W. H.; Mosca, D. H., Valence Evaluation of Cerium in Nanocrystalline CeO_2 Films Electrodeposited on Si Substrates. *J. Electrochem. Soc.* **2012,** *159*, K27-K33.

29. Fonda, E.; Andreatta, D.; Colavita, P. E.; Vlaic, G., EXAFS analysis of the L3 edge of Ce in CeO_2: effects of multi-electron excitations and final-state mixed valence. *J. Synchrotron Radiat.* **1999,** *6*, 34-42.

30. Gleaves, J. T.; Yablonskii, G. S.; Phanawadee, P.; Schuurman, Y., TAP-2: An interrogative kinetics approach. *Appl. Catal. A:Gen.* **1997,** *160*, 55-88.

31. Zheng, B.; Hua, W. M.; Yue, Y. H.; Gao, Z., Dehydrogenation of propane to propene over different polymorphs of gallium oxide. *J. Catal.* **2005,** *232*, 143-151.

32. Chen, M. A.; Xu, J.; Cao, Y.; He, H. Y.; Fan, K. N.; Zhuang, J. H., Dehydrogenation of propane over In_2O_3-Al_2O_3 mixed oxide in the presence of carbon dioxide, *J. Catal.* **2010,** *272,* 101-108.

33. Michorczyk, P.; Ogonowski, J.; Kustrowski, P.; Chmielarz, L., Chromium oxide supported on MCM-41 as a highly active and selective catalyst for dehydrogenation of propane with CO_2, *Appl. Catal. A:Gen.* **2008,** *349*, 62-69.

34. Moulijn, J. A.; van Diepen, A. E.; Kapteijn, F., Catalyst deactivation: is it predictable? What to do? *Appl. Catal. A:Gen.* **2001,** *212*, 3-16.

35. Bhasin, M. M.; McCain, J. H.; Vora, B. V.; Imai, T.; Pujado, P. R., Dehydrogenation and oxydehydrogenation of paraffins to olefins., *Appl. Catal. A:Gen.* **2001,** *221*, 397-419.

36. Yashima, M.; Arashi, H.; Kakihana, M.; Yoshimura, M., Raman Scattering Study of Cubic–Tetragonal Phase Transition in $Zr_{1-x}Ce_xO_2$ Solid Solution. *J. Am. Ceram. Soc.* **1994,** *77*, 1067-1071.

37. Kishimoto, H.; Omata, T.; Otsuka-Yao-Matsuo, S.; Ueda, K.; Hosono, H.; Kawazoe, H., Crystal structure of metastable κ-$CeZrO_4$ phase possessing an ordered arrangement of Ce and Zr ions. *J. Alloys Compd.* **2000,** *312,* 94-103.

38. Acuna, L. M.; Lamas, D. G.; Fuentes, R. O.; Fabregas, I. O.; Fantini, M. C. A.; Craievich, A. F.; Prado, R. J., Local atomic structure in tetragonal pure ZrO_2 nanopowders. *J. Appl.Crystallogr.* **2010,** *43*, 227-236.

39. Nagai, Y.; Yamamoto, T.; Tanaka, T.; Yoshida, S.; Nonaka, T.; Okamoto, T.; Suda, A.; Sugiura, M., XAFS and XRD analysis of ceria-zirconia oxygen storage promoters for automotive catalysts. *Top. Catal.* **2008,** *47*, 137-147.

40. Kou, Y.; Su, G.-q.; Zhang, W.-z.; Yin, Y.-q., Investigation of the Ensemble Effect of ZrO_2/Al_2O_3 Catalyst on Selective Synthesis of Ethylene from CO and H_2, *J. Catal.* **1996,** *162,* 361-364.

41. Vlaic, G.; Di Monte, R.; Fornasiero, P.; Fonda, E.; Kaspar, J.; Graziani, M., Redox property-local structure relationships in the ph-loaded CeO2-ZrO2 mixed oxides. *J. Catal.* **1999,** *182,* 378-389.

42. Nachimuthu, P.; Shih, W. C.; Liu, R. S.; Jang, L. Y.; Chen, J. M., The study of nanocrystalline cerium oxide by X-ray absorption spectroscopy. *J. Solid State Chem.* **2000,** *149*, 408-413.

43. Fink, H. J.; Grünfeld, V.; López, A., Quantum-interference device without Josephson junctions. *Phys. Rev. B* **1987,** *35*, 35-37.

44. Atanga, M. A.; Rezaei, F.; Jawad, A.; Fitch, M.; Rownaghi, A. A., Oxidative dehydrogenation of propane to propylene with carbon dioxide. *Appl. Catal. B: Environ.* **2018,** *220*, 429-445.

45. Miao, J. Y.; Yang, L. F.; Cai, J. X., Acidities of CeO_2 and $Ce_{0.5}Zr_{0.5}O_2$ solid solutions studied by NH_3-TPD. *Surf. Interface Anal.* **1999,** *28*, 123-125.

46. Fornasiero, P.; Balducci, G.; Di Monte, R.; Kašpar, J.; Sergo, V.; Gubitosa, G.; Ferrero, A.; Graziani, M., Modification of the Redox Behaviour of CeO_2 Induced by Structural Doping with ZrO_2, *J. Catal.* **1996,** *164*, 173-183.

47. Šesták, J.; Berggren, G., Study of the kinetics of the mechanism of solid-state reactions at increasing temperatures. *Thermochim. Acta* **1971,** *3*, 1-12.

48. Munteanu, G.; Ilieva, L.; Nedyalkova, R.; Andreeva, D., Influence of gold on the reduction behaviour of Au–V_2O_5/CeO_2 catalytic systems: TPR and kinetic parameters of reduction., *Appl. Catal. A:Gen.* **2004,** *277*, 31-40.

49. Chou, C.-W.; Chu, S.-J.; Chiang, H.-J.; Huang, C.-Y.; Lee, C.-j.; Sheen, S.-R.; Perng, T. P.; Yeh, C.-t., Temperature-Programmed Reduction Study on Calcination of Nano-Palladium. *J. Phys. Chem. B* **2001,** *105*, 9113-9117.

50. Lan, L.; Chen, S.; Cao, Y.; Gong, M.; Chen, Y., New insights into the structure of a CeO_2-ZrO_2-Al_2O_3 composite and its influence on the performance of the supported Pd-only three-way catalyst. *Catal. Sci. Tech.* **2015,** *5*, 4488-4500.

51. Staudt, T.; Lykhach, Y.; Tsud, N.; Skála, T.; Prince, K. C.; Matolín, V.; Libuda, J., Ceria reoxidation by CO2: A model study, *J. Catal.* **2010,** *275*, 181-185.

52. Sasmaz, E.; Wang, C.; Lance, M. J.; Lauterbach, J., In situ spectroscopic investigation of a Pd local structure over Pd/CeO_2 and Pd/MnO_x-CeO_2 during CO oxidation. *J. Mater. Chem. A* **2017,** *5*, 12998-13008.

53. Gutiérrez-Ortiz, J. I.; de Rivas, B.; López-Fonseca, R.; González-Velasco, J. R., Characterization of the catalytic properties of ceria-zirconia mixed oxides by temperature-programmed techniques. *J. Therm. Anal. Calorim.* **2005,** *80*, 225-228.

54. Ohishi, Y.; Kawabata, T.; Shishido, T.; Takaki, K.; Zhang, Q.; Wang, Y.; Takehira, K., Dehydrogenation of ethylbenzene with CO_2 over Cr-MCM-41 catalyst. *J. Mol. Catal. A: Chem.* **2005,** *230*, 49-58.

55. Michorczyk, P.; Pietrzyk, P.; Ogonowski, J., Preparation and characterization of SBA-1–supported chromium oxide catalysts for CO_2 assisted dehydrogenation of propane. *Micropor. Mesopor. Mat.* **2012,** *161*, 56-66.

56. Carley, A. F.; Davies, P. R.; Roberts, M. W., Oxygen transient states in catalytic oxidation at metal surfaces. *Catal. Today* **2011,** *169*, 118-124.

57. Haber, J., Molecular Description of Transition Metal Oxide Catalysts. In *Surface Chemistry and Catalysis*, Carley, A. F.; Davies, P. R.; Hutchings, G. J.; Spencer, M. S., Eds. Springer US: Boston, MA, 2002; pp 275-293.

58. Golunski, S.; Rajaram, R.; Hodge, N.; Hutchings, G. J.; Kiely, C. J., Low-temperature redox activity in co-precipitated catalysts: a comparison between gold and platinum-group metals. *Catal.Today* **2002,** *72*, 107-113.

59. Acerbi, N.; Tsang, S. C. E.; Jones, G.; Golunski, S.; Collier, P., Rationalization of Interactions in Precious Metal/Ceria Catalysts Using the d-Band Center Model. *Angew. Chem., Int. Ed.* **2013,** *52*, 7737-7741.

60. Golunski, S. E.; Walker, A. P., Mechanism of low-temperature oxydehydrogenation of 1-butene to 1,3-butadiene over a novel Pd-Fe-O catalyst, *J. Catal.* **2001,** *204*, 209-218.

For Table of Contents Only: Graphical Abstract (size 4.25cm x 6.89cm)